Scientific Data

https://doi.org/10.1038/s41597-026-06564-1

Article in Press

Human brain MRI data of intrathecally injected tracer evolution over 72 hours for data-integrated simulations

Received: 4 August 2025

Accepted: 6 January 2026

Cite this article as: Riseth, J.N., Koch, T., Lian, S.L. *et al.* Human brain MRI data of intrathecally injected tracer evolution over 72 hours for data-integrated simulations. *Sci Data* (2026). https://doi.org/10.1038/s41597-026-06564-1

Jørgen N. Riseth, Timo Koch, Sofie Lysholm Lian, Tryggve Holck Storås, Ludmil T. Zikatanov, Lars Magnus Valnes, Kaja Nordengen & Kent-André Mardal

SCIENTIFIC DATA

CONFIDENTIAL
COPY OF SUBMISSION FOR PEER REVIEW ONLY

Tracking no: SDATA-25-04432A

Human brain MRI data of CSF tracer evolution over 72h for data-integrated simulations

Authors: Kent-Andre Mardal (Simula Research Laboratory), Jørgen Riseth (Simula Research Laboratory), Timo Koch (Simula Research Laboratory), Sofie Lian (University of Oslo), Tryggve Storås (Oslo University Hospital), Ludmil Zikathanov (Penn State University), Lars Magnus Lars Magnus (University of Oslo), and Kaja Nordengen (Oslo University Hospital)

Abstract:
We present the Gonzo dataset: Brain MRI and derivative data from one healthy male human volunteer (“Gonzo”) before and during the 72 hours after intrathecal injection of the contrast agent gadobutrol into the cerebrospinal fluid (CSF) of the spinal canal. The MRI data records include images highlighting the temporal and spatial evolution of the contrast agent in CSF, brain, and adjacent structures. In addition to raw MRI, we provide derivatives that enable numerical simulations of the transport process under study. Derivatives include T_1 maps, tracer concentration maps, diffusion tensor maps, and unstructured triangulated volume meshes of the brain geometry. We also provide brain region markers obtained by image segmentation. A regional statistical analysis of the concentration data complements the image data. The presented data can be used to study the transport behavior and the underlying processes of a tracer in the brain. It is intended to contribute to and inspire new studies on the understanding of tracer transport, method development for image analysis, and simulation of brain fluid transport processes.

Datasets:

Repository Name	Dataset Title	Accession Number or DOI	URL to data record	Private reviewer access URL/code
Zenodo	The Gonzo Dataset: Human Brain MRI Data of CSF Tracer Evolution Over 72h For Data-Integrated Simulations	10.5281/zenodo.14266866	https://doi.org/10.5281/zenodo.14266866	

Human brain MRI data of intrathecally injected tracer evolution over 72 hours for data-integrated simulations

Jørgen N. Riseth[1], Timo Koch[1,2,3], Sofie Lysholm Lian[4], Tryggve Holck Storås[5], Ludmil T. Zikatanov[2,6], Lars Magnus Valnes[2], Kaja Nordengen[4,5], and Kent-André Mardal[1,2,7,†]

[1]Scientific Computing and Numerical Analysis (SCAN), Simula Research Laboratory, Oslo, Norway
[2]Department of Mathematics, University of Oslo, Oslo, Norway
[3]Department of Hydromechanics and Modelling of Hydrosystems, University of Stuttgart, Stuttgart, Germany
[4]Institute of Clinical Medicine, University of Oslo, Oslo, Norway
[5]Department of Neurology, Oslo University Hospital, Oslo, Norway
[6]Department of Mathematics, The Pennsylvania State University, University Park, USA
[7]KG Jebsen Center for Brain Fluid Research, Oslo, Norway
[†]Corresponding author: kent-and@simula.no

Abstract

We present the Gonzo dataset: Brain MRI with processed and derivative data from one healthy male human volunteer ("Gonzo") before and during the 72 hours after intrathecal injection of the contrast agent gadobutrol into the cerebrospinal fluid (CSF) of the spinal canal. The MRI data records include images highlighting the temporal and spatial evolution of the contrast agent in CSF, brain, and adjacent structures. In addition to raw MRI, we provide derivatives that enable numerical simulations of the transport process under study. Derivatives include T_1 maps, tracer concentration maps, diffusion tensor maps, and unstructured triangulated volume meshes of the brain geometry. We also provide brain region markers obtained by image segmentation. A regional statistical analysis of the concentration data complements the image data. The presented data can be used to study the transport behavior and the underlying processes of a tracer in the brain. It is intended to contribute to and inspire new studies on the understanding of tracer transport, method development for image analysis, and simulation of brain fluid transport processes.

Background & Summary

Cerebrospinal fluid (CSF) surrounds the brain and spinal cord, in the subarachnoid space, and in the ventricular system. The motion of the CSF is dynamic and complex; fluid is secreted in the choroid plexus in the ventricles; the flow of the CSF is also pulsatile with several relevant frequencies driven by heart[1], respiration[2], vasomotion[3], and sleep cycles[4]. Apart from acting as a shock absorber for the brain, CSF offers a potential route for drug delivery to the brain, circumventing the blood-brain barrier that hinders most blood-borne substances from reaching the functional brain tissue. CSF is also proposed to be crucial for waste clearance[5;6] from brain tissue, which lacks a lymphatic system. The glymphatic hypothesis proposes that a brain-wide system connecting the CSF and brain extracellular space through perivascular spaces[5] clears waste, in particular during sleep[6]. The mechanisms behind such clearance are partially unknown[7] and may be multi-faceted. A variety of theoretical and computational models proposing driving mechanisms for waste include explanations based on peristalsis-driven netflow[8–11], dispersion[12;13], multi-compartment diffusion-reaction models[14], or multiple network poroelasticity [15;16]. However, the driving mechanisms are still being debated, with no mechanistic model able to explain the variety of clinically and experimentally observed transport phenomena[7;17].

Few methods today can probe fluid transport in humans. A method for assessing the transport of substances in the CSF and brain is dynamic contrast-enhanced magnetic resonance imaging (MRI): a contrast agent (CA) is

Figure 1: **Human brain MRI of CSF tracer evolution over 72h** The dataset contains head images from (contrast-enhanced) magnetic resonance imaging (MRI) with intrathecal injection of contrast agent (CA); the data collection protocol is visualized in the figure. The CA (gadobutrol) spreads along the spinal canal into the cerebrospinal fluid (CSF) spaces in and around the brain. MR images with different MR sequences (Table 5) are acquired at four subsequent time points as well as before contrast administration (session duration ≈ 30 min and ≈ 1 h pre-contrast). Blood samples are taken between MRI acquisitions and analyzed for CA plasma concentration.

injected intrathecally (into the CSF-filled spaces in the spinal canal of the lower back), and the brain is imaged over several days using a combination of multiple MRI sequences[18–29], see Fig. 1. The CA shortens the longitudinal and transversal relaxation times, T_1 and T_2, such that their reciprocal relaxation rates, $R_1 = 1/T_1$ and $R_2 = 1/T_2$, increase by an amount proportional to the concentration of the CA. The concentration of the CA can thus be visualized as contrast images, using appropriate MR sequences, as further described in section Methods.

Intrathecal contrast-enhanced MRI (also called "glymphatic MRI"[22]) is an off-label use of MR contrast agents[30], relatively time-consuming ($\approx$ 30 min per session for multiple sequences recorded), invasive (CA administration), and typically restricted to patients with underlying CSF pathologies. Although considered safe when using low doses of gadolinium-based contrast medium[25;31;32], human studies are scarce. MRI data from clinical research projects using glymphatic MRI are not accessible to the public due to privacy concerns and ethical considerations. However, access to image data is crucial for designing data analysis pipelines and three-dimensional, subject-specific computational simulations. These tools support understanding the underlying physics of the complex transport phenomena visualized. For the first time, we can provide such data as a publicly accessible dataset.

A healthy volunteer participant in a recently started clinical study (see GRIP in Section Methods) on the role of glymphatic clearance in proteinopathies (such as Parkinson's disease) provided informed consent to conducting a glymphatic MRI study and making the data publicly available. The dataset resulting from the collection procedure shown in Fig. 1 is intended as a data source in data-integrated simulation techniques to research and "reverse-engineer" transport mechanics; it also serves as a starting point to develop data processing frameworks working with glymphatic MRI, or similar data.

An apparent drawback of the presented dataset is that it only contains data from a single individual. Previous studies using glymphatic MRI have shown large inter-individual differences in CSF transport patterns[33]. Hence, the dataset alone does not enable physiological or medical conclusions based on statistics. The dataset is, however, valuable in another way: while data from a single subject is insufficient to construct purely data-driven models, physics-based computational and mathematical modelers can still effectively use the dataset for validation purposes and testing of mechanistic hypothesis; physics-based models emulate the actual transport process in between sparse data. Moreover, a dataset with a single subject also allows for a controlled and repeatable environment for patient-specific method development based on clinical non-synthetic data.

In summary, the purpose of the present dataset is to provide data and simulation scientists with a comprehensive, openly available contrast-enhanced MRI dataset, enabling testing and validation of computational models of solute transport in the brain. Since for the development of mathematical models, quantitative measurements are crucial—even if sparse—we provide blood sample measurements acquired between MRI sessions, cf. Fig. 1 supplementing the raw MRI data. Finally, various post-processing tools and post-processed data that allow the direct use of the data in mesh-based computational simulations are presented.

Methods

Inclusion and clinical procedure

A healthy male volunteer in his 60s was recruited for study. He underwent a thorough neurological examination and cognitive tests, which were normal. An MRI examination revealed no more than non-specific white matter hyperintensities and a tendency towards iron deposition in the basal ganglia. Dementia markers in the cerebrospinal fluid were within the normal range (amyloid beta, total tau, and pTau181). Using X-ray guidance, an interventional radiologist performed a lumbar puncture in the lateral position with a thin (G25) atraumatic needle. Proper needle placement was confirmed through the passive release of cerebrospinal fluid, after which an MRI contrast agent (0.25 mmol of gadobutrol, 1 mL) was administered intrathecally. MRI acquisitions were carried out 4.5 h, 1 d (25 h), 2 d (49 h), 3 d (70 h) after contrast agent administration, in addition to pre-contrast MRI.

The study obtained approval from the Regional Ethics Committee (REC #282297) and the Hospital Authority (Data Protection approval #21/19051). The healthy volunteer provided written and oral informed consent, both for participating in the study and for the open-access publication of the full series of MRI scans as part of this publication.

Blood plasma concentration measurements

Intravenous blood samples were obtained at nine different timepoints, and quantification of gadolinium (Gd) in the blood samples were performed by the climate and environmental research institute NILU (Kjeller, Norway),

using inductively coupled plasma mass spectrometry, as previously described in [34]. The concentration measurement data points are provided in milligram gadolinium per kilogram plasma. For convenience, we converted the values to molar concentrations of gadobutrol using a plasma density of $1025\,\mathrm{kg\,m^{-3}}$, $157.3 \times 10^{-3}\,\mathrm{kg\,mol^{-1}}$, and the fact that each gadobutrol molecule contains one gadolinium atom. The results are presented in Table 4. The raw and converted data is included in the dataset (see Data Records).

MRI data acquisition

The MRI scans acquired include T_1-weighted images, a Look-Locker sequence, and a T2-weighted mixed inversion recovery, spin-echo sequence (Mixed) sequence [35] in all sessions, and T_2-weighted images, FLAIR, and diffusion tensor imaging (DTI) in the pre-contrast session. Scanning was performed on a 3 T Philips Ingenia MRI scanner (Philips Medical Systems, Best, The Netherlands) with a 32-channel head coil. The MRI Sequence parameters are summarized in Table 5. Pre-contrast session sample images are shown in Fig. 2.

MRI file format

The image data in this dataset are provided in the NIfTI 1 format. The NIfTI files are obtained by converting the scanner-native Philips-enhanced DICOM format files using the software `dcm2niix` [36](`https://github.com/rordenlab/dcm2niix`). Associated with each NIfTI file is a Brain Image Data Structure (BIDS) file containing metadata in JSON format. Images from the Mixed sequence were converted from Philips-enhanced DICOM to NIfTI using a custom script (see Section Data Records). The script was verified by ensuring it outputs the same floating point values and affine map as `dcm2niix` for a T_1-weighted image.

Estimating T_1 times from Look-Locker sequences

T_1 maps for brain tissue are generated voxel-wise by fitting a curve to the longitudinal magnetization recovery signal from a Look-Locker image sequence [37] as shown in Fig. 3(a) for the pre-contrast session. The tissue's net magnetic moment is flipped anti-parallel to the MRI's main magnetic field. Following the inversion of magnetic moments, the longitudinal magnetization is expected to follow a curve

$$M(t) = M_0\,(1 - 2\exp(-t/T_1))\,. \tag{1}$$

However, due to imperfect inversion of the magnetic field, measurement errors, and disturbances induced by signal generation, the T_1 times are typically found by fitting a curve [38]

$$f(t) = A - B\exp(-t/T_1^*), \quad \text{with} \quad T_1 = T_1^*\left(\frac{B}{A} - 1\right) \tag{2}$$

to the measured signal intensities for the generic parameters A, B and where T_1^* denotes the *apparent* T_1 time [38]. Instead of directly fitting the above curve to the signal intensities, we reparametrize it to include apriori knowledge about the expected shape and form of the curve,

$$f(t) = x_1(1 - (1 + x_2^2)e^{-x_3^2 t}), \quad \text{with} \quad A = x_1, \quad B = x_1(1 + x_2^2), \quad T_1^* = x_3^{-2}, \quad T_1 = x_2^2 x_3^{-2}. \tag{3}$$

This parametrization guarantees a sign flip for $t \geq 0$ and a positive T_1 time. The signal intensity time series $\{\hat{S}_{t_1}, \ldots, \hat{S}_{t_N}\}$ (here $N = 14$) in the Look-Locker sequence images included in this dataset represent the magnitude of the complex longitudinal magnetization value; they are thus positive, cf. Fig. 3(b). Therefore, we fit $|f(t)|$ to the 14 data points per voxel, which we normalize by their local (voxel-wise) maximum value over time to ensure similar order of magnitude. We use `scipy.optimize.curve_fit` from the SciPy-library [39] using the Levenberg-Marquardt algorithm. To avoid outliers, we additionally treated extreme values. Voxel values were voided (set to NaN) either before or during the relaxation analysis if either $\max\{\hat{S}_{t_j}, \ldots, \hat{S}_{t_N}\} = 0$, the optimization algorithm does not converge within less than 1000 function evaluations, or if the optimization algorithm raises an exception. After T_1 estimation, we voided voxels with estimated T_1 times outside of the range $[50, 5000]$ ms. Finally, any voided voxels within the head were interpolated from the surroundings. A sagittal view of the resulting T_1 map is shown in Fig. 4.

Estimating T_1 times from the Mixed sequence

The Lock-Locker estimation yields poor results (see Section Technical Validation) if the data acquisition period is much shorter than the T_1 relaxation time of the sample (see, for instance, the green curve (ventricular CSF) in Fig. 3(b), which at the end of the acquisition period is still far from equilibrium magnetization). Longer acquisition periods are technically possible but lead to longer MRI sessions (the Lock-Locker sequence with a data acquisition time of 2750 ms takes ≈ 12 min, cf. Table 5) possibly causing patient discomfort.

The mixed inversion recovery and spin echo sequence (Mixed), introduced in [35], is designed to enable the estimation of long T_1 times (e.g., CSF) more accurately and faster than with the Look-Locker sequence. Two images are acquired: a spin echo signal with signal S_{SE} and an image inversion recovery image with signal S_{IR}. The signals are estimated by

$$S_{\mathrm{SE}}(T_1) = M_0 \left(1 - e^{-\frac{\mathrm{TR}}{T_1}}\right), \quad S_{\mathrm{IR}}(T_1) = M_0 - (M_0 + S_{\mathrm{SE}})e^{-\frac{\mathrm{TI}}{T_1}}, \tag{4}$$

where M_0 is the equilibrium magnetization of the tissue, TI is the inversion time, and TR is the repetition time [40]. To estimate T_1 maps from these two signals, one observes that the ratio

$$f(T_1) = \frac{S_{\mathrm{IR}}(T_1)}{S_{\mathrm{SE}}(T_1)} = \frac{1 - \left(2 - e^{-\frac{T_R}{T_1}}\right) e^{-\frac{TI}{T_1}}}{1 - e^{-\frac{TR}{T_1}}}. \tag{5}$$

is a monotonically decreasing function and therefore invertible: by computing the ratio $f(T_1)$ from measured data, we can get T_1 by solving the nonlinear Eq. (5).

The T_1 times estimated from the Mixed sequence data are accurate for high T_1 values (CSF, low tracer concentration) but become increasingly inaccurate for low T_1 (gray matter or high tracer concentration); see Section Technical Validation. To only retain T_1 estimates for fluid-filled spaces with low contrast, a mask was generated by applying Yen's thresholding algorithm [41] to the spin echo images. T_1 values in voxels outside this mask were voided (set to `NaN`). Figure 4 shows the estimated T_1 maps after masking for each session.

Registration

All images were registered and resampled to the image space of the pre-contrast T_1-weighted image using the software `greedy` [42] (`https://github.com/pyushkevich/greedy`) for rigid registration of images. Rigid registration of an input image to a target image results in a 4×4 matrix representing an affine transformation in homogeneous form for reuse. We used the default parameters of the registration software except for the following MRI-sequence-specific modifications: The pre-contrast T_2-weighted images were registered directly to the target space using a normalized mutual information (NMI) loss function. Each of the post-contrast T_1-weighted images was registered directly to the pre-contrast T_1-weighted image, using a normalized cross-correlation (NCC) loss function with a $5 \times 5 \times 5$ neighborhood. The Look-Locker T_1 maps were resampled to the target space by first registering the corresponding inverted T_1 map images to the target space using an NCC $5 \times 5 \times 5$ loss function and then applying the output transformation to the T_1 maps. The T_1 maps estimated from the Mixed sequence were resampled to the target space by first registering the mixed spin-echo volume to the T_2-weighted image using an NCC loss function with a $5 \times 5 \times 5$ neighborhood and applying the output transformation to the T_1 maps. Following tensor reconstruction, the mean diffusivity was registered to the pre-contrast T_1-weighted image. Finally, the DTI data was resampled to the target space by first registering the estimated mean diffusivity image to the already registered T_2-weighted image, with the NMI loss function. The estimated transform from the preceding step was then used to resample the mean-diffusivity, fractional anisotropy, eigenvalues, and eigenvectors into the image space of the pre-contrast T_1-weighted image. Since greedy only works with 3D MRI data, the eigenvectors are split into components, resampled component-wise, merged to a 4D structure, and renormalized to unit vectors. The resampled eigenvectors and eigenvalues were then used to reconstruct the symmetric diffusion tensors in the target space, with all nine components stored row-wise.

Hybrid T_1 maps

The T_1 times estimated from the Mixed sequence are expected to be most accurate for high T_1 values (e.g., CSF-filled spaces such as the subarachnoid space and the ventricles), whereas the Look-Locker estimates are suitable for small T_1 (e.g., brain tissue and high tracer concentrations). To distinguish CSF from tissue, we created a CSF

mask M_{CSF}. The mask was created using Yen's thresholding method[41] (binary segmentation) on the pre-contrast T_2-weighted image (Fig. 2 middle pane) registered and resampled into the reference image space. After binary segmentation, we discarded all but the largest connected region. While the Mixed sequence is designed for large T_1 times of pre-contrast CSF ($> 4\,\mathrm{s}$), the contrast agent reduces T_1 significantly. Post-contrast T_1 times can reach values well below 1 s in CSF regions with high contrast agent concentrations. Based on the analysis described in Section Technical Validation, we choose a threshold of $T_1 = 1500\,\mathrm{ms}$ to create the hybrid T_1 map

$$T_1 = \begin{cases} T_1^m & M_{CSF} = 1 \text{ and } T_1^{LL} > 1500\,\mathrm{ms} \text{ and } T_1^m > 1500\,\mathrm{ms} \\ T_1^{LL} & \text{otherwise,} \end{cases} \tag{6}$$

where T_1^{LL} and T_1^m denote the registered T_1 maps estimated from Look-Locker and the Mixed sequence, respectively. Figure 4 (third row) shows the hybrid T_1 map for the pre-contrast session. The hybrid map is used to estimate tracer concentrations.

Concentration estimation

Tracer concentrations C are estimated voxel-wise from the hybrid T_1 maps for each session, based on the relation

$$\frac{1}{T_1} = \frac{1}{T_{10}} + r_1 C \tag{7}$$

where T_{10} is the native T_1 time of a given voxel, and $r_1 = 3.2\,\mathrm{s}^{-1}\,\mathrm{L\,mmol}^{-1}$ is the T_1 relaxivity, estimated in[43]. Since we are only interested in intracranial concentrations, we mask the voxels outside the cranium: starting with the binary segmentations of the CSF and the brain, denoted M_{CSF} and M_B, respectively, we create an initial background mask by inverting the union of CSF and brain segmentations. Next, the largest island is extracted from the background mask to remove potential gaps between the CSF and brain segmentations. Finally, we use a binary opening algorithm with a ball of radius 3 as the structuring element. The concentrations estimated from the hybrid Look-Locker/Mixed T_1 maps are shown for each session in Fig. 4.

Diffusion tensor images

The dataset contains dynamic diffusion tensor images (15 directions, $b = 0$ and $1000\,\mathrm{s\,mm}^{-2}$, AP) from 10 different time points. The images were initially corrected for susceptibility distortions and eddy-currents using FSL's[44] `topup`[45;46], and `eddy`[47]. After initial correction, the eigenvalues and eigenvectors of the diffusion tensors were estimated using `dtifit`. Figure 5 shows the mean-diffusivity, fractional anisotropy, and color-coded fractional anisotropy after registration (color-coded fractional anisotropy is an RGB image with RGB-channels $FA \times (|V_{1x}|, |V_{1y}|, |V_{1z}|)$ for the normalized principal eigenvector V_1). Finally, the diffusion image was checked for invalid diffusion tensors based on whether any eigenvalue is negative or whether the fractional anisotropy lies outside the valid range $[0, 1]$; invalid tensors were replaced by the nearest valid diffusion tensor. We refer to[48] Chapter 5 for further details on the post-processing steps.

Normalization of T_1-weighted images

Normalized, post-contrast, T_1-weighted images have previously been used to investigate tracer enrichment in brain tissue following intrathecal injection of contrast agent in a range of studies[22;23;27;33;49]. Following the strategy in[50], the images were normalized by scaling the signals relative to the median signal in a reference region in the (left) orbital eye fat. To automatically generate the reference region, we identified three regions (1012: `ctx-lh-lateralorbitofrontal`; 1027: `ctx-lh-rostralmiddlefrontal`; 1033: `ctx-lh-temporalpole`) from the FreeSurfer segmentation `aparc+aseg.mgz`, one for each coordinate axis and manually align them with the reference regions in the direction of their respective coordinate axes. From these regions, a point in the vicinity of the left orbital fat was found by intersecting the three planes, which lie perpendicular to the coordinate axes and pass through the corresponding FreeSurfer region. The intersecting point was used as the center of a multivariate Gaussian probability distribution with a diagonal covariance matrix chosen such that most of the orbital eye fat is assigned a high probability density, as shown in Fig. 7(a). The distribution was multiplied with the signal intensities of the T_1-weighted image, leaving a focused view of the original image, as shown on the left of Fig. 7(b). Thereafter, a first estimate of the reference region was generated by using Yen's thresholding algorithm[41] implemented in `skimage.morphology`. As a post-processing step, we applied binary erosion to the binary segmentation

and removed all but the largest island. This procedure was performed for the T_1-weighted image from each session (after registration to the pre-contrast image), and the final reference region was taken as the intersection between the reference regions generated from each image.

Cortical reconstruction and segmentation

FreeSurfer's[51] cortical reconstruction pipeline `recon-all` (FreeSurfer version 7.4.1) was used to create surfaces for generating the finite element mesh and segmenting the different regions of the subject's brain. The FreeSurfer-based pipeline was run for the pre-contrast session, taking the T_1-weighted image as main input (as shown in the leftmost image in Fig. 6, together with the FLAIR image which helps with the pial surface reconstruction. Brain segmentation has two main purposes: First, it enables us to compute region-specific quantities, such as total tracer mass within a specific region, allowing for quantitative analysis of tracer movements. Second, segmentation forms the basis for boolean arrays, which allow us to process brain tissue differently from CSF-filled spaces. We also include the output of the FastSurfer pipeline, a fully compatible FreeSurfer alternative, using deep learning for segmentation and a spectral projection algorithm for surface reconstruction[52].

Mesh generation

A 3D computational mesh (tetrahedral volume mesh) of the cerebrum, as shown in Fig. 8, was generated using a process based on the one described in[48] Ch. 4. The process relies on surface meshes of the ventricles, subcortical gray matter, the pial surface, and surfaces for the interface between the gray and white matter. The pial and white matter surfaces (for each hemisphere) were created by the FreeSurfer `recon-all` pipeline. The ventricles (as shown in Fig. 8(c)) and subcortical gray matter surfaces were extracted as contour surfaces based on the FreeSurfer segmentation `aseg.mgz`. After meshing, the ventricles were removed, so only the brain tissue remains. The subcortical gray matter structures can be seen in the subdomain labels of Fig. 8(b). The pre-processing of surfaces and the mesh generation uses the Python libraries `pyvista`[53] and `SVMTK`(`https://github.com/SVMTK/SVMTK`). Further details on the procedure may be found in the script `src/brainmeshing/mesh_generation.py` in the repository `https://github.com/jorgenriseth/gMRI2FEM` (also see Section Code Availability).

Mapping FreeSurfer segmentation data onto the mesh

The mesh can be subdivided into subdomains corresponding to the FreeSurfer segmentation data such as shown in Fig. 8(c–f) for the `aseg+aparc`-segmentation. Each cell is labeled according to the most common label in the voxels in a neighborhood around the cell midpoint, with an additional check to ensure that each label is contained within only one of the subdomains illustrated in Fig. 8(b) originating from the meshing procedure. We refer to[48] chapter 4 for further details.

Mapping function data onto the mesh

Mesh vertices are associated with two types of concentration data: one representing the concentration field within the CSF at the brain surface and one representing the tissue concentrations within the brain. Both can be represented as piecewise-linear, continuous finite element functions across the entire domain (setting inner nodes to zero for the surface data).

The surface concentration data is intended to be used to derive boundary conditions for mesh-based transport simulations. The degrees of freedom of the basis functions that are associated with the boundary vertices are assigned the median concentration of the ten nearest voxels within the CSF, as defined by the previously described CSF mask. All internal degrees of freedom are assigned 0. The surface concentration for all sessions is shown in Fig. 9. The internal concentrations u are mapped from the MRI-image C by an approximate Galerkin projection onto the space of continuous, piecewise linear functions V_h on the mesh Ω_h. The Galerkin projection is done by solving the variational problem

$$\int_{\Omega_h} uv \, \mathrm{dx} = \int_{\Omega_h} Cv \, \mathrm{dx} \quad \forall v \in V_h \tag{8}$$

where we interpret C as a piecewise constant function on a quadrilateral mesh containing the brain mesh Ω_h. The assembly of the algebraic system corresponding to the variational equation (8) entails using a numerical quadrature

rule for each cell in the mesh. We approximate the right hand side of the variational form using Gaussian quadrature with quadrature degree 6.

In addition to the concentrations, data from DTI are also included with the mesh. The data includes mean diffusivity, fractional anisotropy, and diffusion tensors. However, these quantities are represented as cell fields, and the values are assigned from the neighborhood of the cell midpoint. The mean diffusivity and fractional anisotropy are assigned the median value of the ten nearest neighbors, whereas the tensors are assigned from the single nearest voxel.

Data Records

All records are available in a Zenodo dataset found at `https://zenodo.org/records/14266867`[54]. The directory structure of the data record roughly indicate the level of processing that the containing files have undergone compared to the the raw data, and may be described as follows:

- `mri_dataset`: Contains MRI-images with metadata converted from the DICOM format, as well as direct derivatives from the individual MRI's. This implies that the image coordinates of images within this folder does not coincide. The directory also contains a time table for each of the sequences relative to the injection time, as well as the tracer concentration measurements from the blood samples.
- `mri_processed_data`: Contains MRI-data and other derivatives of the MRI images which is incompatible with the BIDS-format, such as a the FreeSurfer/FastSurfer-output, or where a non-BIDS directory structure were deemed more suitable.
- `mri_processed_data/sub-01`: Includes co-registered MR-images, T_1-maps, concentration maps, segmentations, computational meshes with associated data and transformation matrices between the different sequences. All of the MRI-images, surfaces and meshes have been co-registered to the reference coordinate space of the pre-contrast T1-weighted image.
- `mri_processed_data/sub-01/modeling`: Contains 3D surfaces and computational meshes with accompanying mesh data, such as concentrations, subdomain tags and diffusion tensors, intended for informing and validating computational models of solute transport in brain tissue.

The different file formats included in the data record, a description of the file format, and an example directory of where to find each of the file-types are listed in Table 1. The data record is split into five different zip-compressed archives, as further detailed below, and enables users to download only a subset of the data depending on their needs.

`mri-dataset.zip` Contains the MRI images output by `dcm2niix` with meta-data.

- `mri_dataset/`
  - `timetable.tsv` - Timetable of MRI sequences given in seconds relative to time of contrast injection.
  - `blood_concentrations.csv` - Gadolinium concentrations measurements from blood plasma samples.
- `mri_dataset/sub-01/ses-01/anat/` - Contains anatomical MRI available only for the pre-contrast session.
  - `sub-01_ses-01_FLAIR{.nii.gz,.json}` - FLAIR MRI with BIDS sidecar.
  - `sub-01_ses-01_T2w{.nii.gz,.json}` - T2-weighted MRI with BIDS sidecar.
- `mri_dataset/sub-01/ses-XX/anat/` - Contains anatomical MRI available only for all 5 sessions.
  - `sub-01_ses-XX_T1w{.nii.gz,.json}` - T1-weighted MRI with BIDS sidecar.
  - `sub-01_ses-XX_acq-looklocker_IRT1{.nii.gz,.json}` - Look-Locker sequence (4D MRI) with sidecar.

  - `sub-01_ses-XX_acq-looklocker_IRT1_trigger_times.txt` - Text file with the trigger times in milliseconds for the corresponding Look-Locker sequence.

- `mri_dataset/sub-01/ses-XX/mixed/` - Contains Mixed data available for all 5 sessions

  - `sub-01_ses-XX_acq-mixed.json` - BIDS sidecar accompanying all mixed MRI data.
  - `sub-01_ses-XX_acq-mixed_IR-corrected-real.nii.gz` - Mixed inversion recovery MRI.
  - `sub-01_ses-XX_acq-mixed_SE-modulus.nii.gz` - Mixed spin-echo MRI.
  - `sub-01_ses-XX_acq-mixed_T1map_scanner.nii.gz` - T1-map generated by scanner from mixed sequence.
  - `sub-01_ses-XX_acq-mixed_meta.json` - Additional metadata needed for T1-map generation from Mixed.

- `mri_dataset/sub-01/ses-01/dwi/` - Contains diffusion-weighted MRI data available only for the pre-contrast session.

  - `sub-01_ses-01_acq-multiband_sense_dir-AP_DTI{.nii.gz,.json,.bval,.bvec}` - Diffusion weighted measurements with BIDS sidecar, and `bval`/`bvec`-files describing strength and direction of the gradient field.
  - `sub-01_ses-01_acq-multiband_sense_dir-AP_DTI_ADC.nii.gz` - Apparent diffusion coefficient output by `dcm2niix`.
  - `sub-01_ses-01_acq-multiband_sense_dir-PA_b0{.nii.gz,.json}` - Reference MRI with BIDS sidecar, taken with opposing phase-encoding direction of the DTI-data for correcting susceptibility induced distortions.

`mri-dataset-precontrast-only.zip` Contains the same data as `mri_dataset.zip`, but only for the pre-contrast session (`ses-01`).

`mri-processed.zip` Contains MRI data derived from the raw data.

- `mri_dataset/derivatives/sub-01/ses-01/dwi/` - Contains DTI-data generated by fitting diffusion tensors using `dtifit`.

  - `sub-01_ses-01_dDTI_FA.nii.gz` - Fractional anisotropy of the diffusion tensors.
  - `sub-01_ses-01_dDTI_L{1,2,3}.nii.gz` - Eigenvalues of the diffusion tensors.
  - `sub-01_ses-01_dDTI_MD.nii.gz` - Mean diffusivity of the diffusion tensors.
  - `sub-01_ses-01_dDTI_V{1,2,3}.nii.gz` - Eigenvectors of the diffusion tensors.
  - `sub-01_ses-01_dDTI_tensor.nii.gz` - 6-component (symmetric) diffusion tensors, ordered (D_xx, D_xy, D_xz, D_yy, D_yz, D_zz).

- `mri_dataset/derivatives/sub-01/ses-XX/` - Contains DTI-data derived directly from the raw images.

  - `sub-01_ses-XX_acq-looklocker_T1map.nii.gz` - T1-map estimated from Look-Locker.
  - `sub-01_ses-XX_acq-looklocker_T1map_nICE.nii.gz` - T1-map estimated from Look-Locker using nordicICE.
  - `sub-01_ses-XX_acq-mixed_T1map.nii.gz` - T1-map estimated from the mixed-sequence.

- `mri_processed_data/sub-01/T1maps/` - Contains combined Look-Locker, Mixed T1-maps.

  - `sub-01_ses-XX_T1map_hybrid.nii.gz` - Hybrid T1-map combining T1maps from Look-Locker and Mixed.

- `mri_processed_data/sub-01/T1w_normalized/` - Contains normalized T1-weighted images.

  - `sub-01_ses-XX_T1w_normalized.nii.gz` - T1-weighted MRI after normalization relative to orbital fat signal.

- `mri_processed_data/sub-01/concentrations/` - Contains concentation data.
  - `sub-01_ses-XX_concentration.nii.gz` - MRI representing intracranial tracer concentrations.
- `mri_processed_data/sub-01/dwi/` - Contains DTI-data processed following registration.
  - `sub-01_ses-01_dDTI_cleaned.nii.gz` - 6-component diffusion tensor after replacement of invalid tensors.
- `mri_processed_data/sub-01/registered/` - Contains MRI data registered to the image space of the reference the pre-contrast T_1-weighted image. All MRI images within `mri_processed_data/sub-01` go via this directory.
  - `sub-01_ses-XX_sequence_registered.nii.gz` - Represent any MRI registered and resliced into the reference space.
- `mri_processed_data/sub-01/segmentations/` - Contains various segmentations of the brain and CSF spaces.
  - `sub-01_seg-aparc+aseg_refined.nii.gz` - FreeSurfer segmentation `aparc+aseg` resampled into reference image space.
  - `sub-01_seg-aseg_refined.nii.gz` - FreeSurfer segmentation `aseg` resampled into reference image space.
  - `sub-01_seg-csf-aparc+aseg.nii.gz` - Segmentation of CSF-space based on nearest neighouring label in `aparc+aseg`.
  - `sub-01_seg-csf-aseg.nii.gz` - Segmentation of CSF-space based on nearest neighouring label in `aparc+aseg`.
  - `sub-01_seg-csf-wmparc.nii.gz` - Segmentation of CSF-space based on nearest neighouring label in `wmparc`.
  - `sub-01_seg-csf_binary.nii.gz` - CSF-mask in reference space.
  - `sub-01_seg-intracranial_binary.nii.gz` - Intracranial mask generated from combining CSF-mask and binary representation of `aseg`.
  - `sub-01_seg-refroi-left-orbital_binary.nii.gz` - Left orbital fat reference region mask.
  - `sub-01_seg-wmparc_refined.nii.gz` - FreeSurfer segmentation `wmparc` resampled into reference image space.
- `mri_processed_data/sub-01/transforms/` - Contains affine transformation matrices used to register and reslice MR images into reference space.
  - `sub-01_ses-XX_sequence.mat` - Affine transformation matrix for reslicing the given MRI sequence into the reference space.

`freesurfer.zip` FreeSurfer-data.

- `mri_processed_data/freesurfer/sub-01/` - Contains output of the FreeSurfer `recon-all`-pipeline. See `https://surfer.nmr.mgh.harvard.edu/fswiki/ReconAllOutputFiles` for further details.

`surfaces.zip`

- `mri_processed_data/sub-01/modeling/surfaces/` - Contains processed surfaces used as input for the `SVMTK` meshing algorithm.
  - `lh_pial.stl` - Left hemisphere pial surface.
  - `rh_pial.stl` - Right hemisphere pial surface.
  - `subcortical_gm.stl` - Subcortical gray matter surfaces.
  - `ventricles.stl` - Ventricular system surfaces.
  - `white.stl` - Merged white-matter surfaces of right and left hemispheres.

`mesh-data.zip`

- `mri_processed_data/sub-01/modeling/resolution32/` - 3D tetrahedral meshes with mapped MRI data.
  - `data.hdf` - FEniCS-compatible HDF5 file with mesh and function-representation of MRI data.
  - `data.vtk` - VTK Legacy Format file (binary) with 3D mesh and mapped MRI data.
  - `data.vtu` - VTK Unstructured Grid XML file (ASCII) with 3D mesh and mapped MRI data.
- `mri_processed_data/sub-01/modeling/resolution32/mesh_xdmfs/` - Contains XDMF files created during the 3D meshing process; for visualization of mesh and subdomain data.
  - `boundaries{.xdmf,.h5}` - XDMF3 file with accompanying HDF5 file containing facet-tags generated during meshing process.
  - `mesh{.xdmf,.h5}` - XDMF3 file with accompanying HDF5 file containing the 3D mesh.
  - `subdomains{.xdmf,.h5}` - XDMF3 file with accompanying HDF5 file showing cell tags generated during meshing process.

We provide post-processing and reuse example code in addition to the main MRI dataset (see Code Availability).

Technical Validation

T_1 estimates

To verify the T_1 times estimated from the Look-Locker sequence, we compare our T_1 map with the T_1 map generated by the software `nordicICE` (`https://crai.no/product/nordicice`). Both maps were registered to the pre-contrast T_1-weighted image. The results are shown in Fig. 10(a). Figure 10(a, inset) shows the distribution of the relative percentage difference between the estimated T_1 times from the two methods, for each session. As part of the Mixed sequence, the proprietary scanner software generates a T_1 map with an upper threshold at 4095 ms and thus misrepresents typical T_1 times of CSF. However, it allows us to verify our T_1 map against another implementation for values below this threshold. A voxel-wise comparison of the estimates is shown for the last session in Fig. 10(b), for which most of the T_1 times of the CSF are below the threshold that is clearly visible as a horizontal line in the data. The mean values and standard deviations of the T_1-estimates for gray matter, white matter, and CSF, and how they compare to previous studies, are listed in Table 3.

To estimate the accuracy of Look-Locker (LL) and Mixed approaches to T_1 time and concentration estimation, we perform an error propagation analysis for the Look-Locker and Mixed post-processing algorithms. From this analysis, we want to motivate the chosen threshold in Eq. (6).

For the Mixed sequence, we model the inversion recovery signal S_{IR} and the spin echo signal S_{SE} as in Eq. (4). Simulated image intensities $\hat{S}_{\mathrm{IR}} = S_{\mathrm{IR}} + \epsilon_{\mathrm{IR}}$ and $\hat{S}_{\mathrm{SE}} = S_{\mathrm{SE}} + \epsilon_{\mathrm{SE}}$ are obtained with TR = 9600 ms, TI = 2650 ms, the error term ϵ_{SE} modeled by a Rayleigh distribution (centered Rice distribution) with standard deviation $\sigma_{\mathrm{SE}} = \max(S_{\mathrm{SE}})/\mathrm{SNR}$, and ϵ_{IR} modeled by a centered normal distribution with standard deviation $\sigma_{\mathrm{IR}} = \max(S_{\mathrm{IR}})/\mathrm{SNR}$. For the Look-Locker sequence, the signal over time is modeled by Eq. (3) setting $x_1 = 1$, $x_2 = 2^{-1/2}$, $x_3 = x_2/T_1$. To obtain simulated signal intensities, we sample the signal at 14 equidistant time points in $T = [0\,\mathrm{ms}, 2600\,\mathrm{ms}]$ and add an error term modeled by a Rayleigh distribution with standard deviation $\max_{t\in T}(f(t))/\mathrm{SNR}$ where we assume that the errors at different time points are uncorrelated. Monte Carlo type simulations are conducted as follows: (1) For 100 different concentrations ("True"), compute the corresponding T_1 times, and simulate 50 signals (for Look-Locker 50 times 14 data points). (2) Estimate T_1 time and concentration ("Estimated") from the simulated data described in Section Methods. For the simulations, we mapped concentrations to T_1 time and vice versa with Eq. (7) assuming $T_{10} = 4500$ ms.

Estimated versus true concentrations and T_1 times for SNR = 25 are shown in Fig. 11. Statistics on the propagated errors are reported in Tables 6 to 9.

Due to the relatively short acquisition time of 2600 ms used for the the Look-Locker sequence, T_1 estimates are increasingly affected by noise with increasing T_1 time. For $T_1 < 1500$ ms and $c > 0.1$ mmol estimates are most accurate. On the other hand, the Mixed sequence is increasingly affected by noise for decreasing T_1 times and increasing concentrations. The concentration estimate appears most accurate for $c < 0.1$ mmol such that the two sequences complement each other.

Concentrations

Studies reporting quantitative concentration estimates following intrathecal injection of gadobutrol in humans are scarce, which precludes a comparison of our estimated concentration values to a body of literature values. Table 2 and Fig. 12 shows the estimated total tracer amount in the brain and CSF in the head for each session. The tracer initially spreads through the CSF-filled spaces with 78.5% of the tracer located in the CSF after 4 h, but after 48 h and 70 h it is spread more evenly. The largest estimated amount of tracer in the head is 11.8×10^{-2} mmol after 24 h, corresponding to 47.2% of the injected total, and the tracer is distributed with 5.19×10^{-2} mmol in the brain and 6.57×10^{-2} mmol in the CSF.

There are several sources of errors with respect to quantitative concentration estimates. The uncertainty related to longitudinal relaxivity, r_1, introduces a source of error in the concentration estimates. Relaxivity depends on the solvent, so we have used a value measured for water at 37 °C of $3.2\,\mathrm{L\,s^{-1}\,mmol^{-1}}$ [43], with similar values of $3.3\,\mathrm{L\,s^{-1}\,mmol^{-1}}$ found in [55]. We could not find the corresponding value measured for CSF, consisting of 99% water [56], but we note that the longitudinal relaxivity for blood plasma, with 92% water, [56] was measured at $4.5\,\mathrm{L\,s^{-1}\,mmol^{-1}}$ [57].

Moreover, we note that the concentration estimates contain negative concentrations. These can be mainly attributed to errors in the T_1 maps, originating from image noise or partial volume effects, particularly at the interface between media with significantly different T_1 times.

Mapping the concentration data from the MRI data voxel representation to the computational mesh introduces additional errors. MRI data may be interpreted as a piecewise-constant function on a regular Cartesian grid, which cannot be represented exactly as a piecewise-linear function on a tetrahedral mesh. As an illustration, Figure 13 shows the original concentration data at 24 h compared to the concentration after first mapping the data to the mesh and then mapping them back.

Diffusion tensor imaging (DTI) data

The mean diffusivity (MD) values for white matter and gray matter are found to be $0.77 \pm 0.17\mathrm{mm}^2/\mathrm{s}$ and $1.05 \pm 0.17\mathrm{mm}^2/\mathrm{s}$, respectively. Due to the low resolution of the DTI, the mean diffusivity of voxels labeled as gray matter is likely to be influenced by their surroundings due to partial volume effects. Table 3 lists previously reported values of the apparent diffusion coefficients (ADC) in human brain tissue. Note that the standard deviation reported for our estimates is not comparable to those reported in the cited literature since they are reporting deviation between mean values for different subjects, whereas we report within-subject variation.

Usage Notes

The complete data records, or the individual zipped archives (as described in Data Records), may be downloaded directly from the online Zenodo repository, found at `https://zenodo.org/records/14266867` [54]. Alternatively, the main code repository related to this manuscript (`gonzo`, see Code Availability) contains a Python script for downloading all, or individual, zipped archives from the data record, using the Zenodo REST API. The repository also contains instructions for producing the entire data record, or specific files, from the raw data. The processing pipeline was developed for computers with an x86_64 architecture running Linux. Example software for opening or viewing the different file types in the data record is listed in Table 1. In addition to the description in this article, many post-processing procedures (and in parts alternative procedures) are described in [48].

We provide additional code that demonstrates how to use parts of the data (post-processed data in the VTK file `mri_processed_data/sub-01/modeling/resolution32/data.vtu`, diffusion tensor images, and the registered anatomical T_1 image data) in a finite-volume tracer transport simulation setup. In particular, this makes clear to users interested in simulation pipelines how to feed the created meshes and parameter fields into a simulation tool and plot the results against MRI reference images for visualization. The code `dumux-braindiffusion-miniapp` is publicly available (see Code availability).

Finally, we note that the MRI dataset provided in this study contains data from a single subject. Consequently, any reuse or analysis of this data should proceed with caution, as the datasets limited scope make it unsuitable for studies requiring representative samples or statistical generalizations. Users are advised to consider these limitations in their applications and avoid overextending the data's implications beyond the presented individual case. However, the data is well-suited for designing simulation pipelines and developing image analysis pipelines for similar types of data and serve as order of magnitude reference.

Data availability

All records are available in the Zenodo repository `https://zenodo.org/records/14266867`[54] with doi:10.5281/zenodo.14266867.

Code availability

The source code for running each step of the described data processing pipeline is split into three repositories. The separation of the source code intends to facilitate the use of the software in future studies involving only parts of the processing pipeline of this dataset.

`gonzo`: The main repository related to this study. It includes instructions for installing necessary dependencies, running the data processing pipeline, and running scripts for creating plots in this document. The code is publicly available at `https://github.com/jorgenriseth/gonzo` and as an archived dataset[58].

`gMRI2FEM`: A Python library used for post-processing MRI data. The code is publicly available at `https://github.com/jorgenriseth/gMRI2FEM` and as an archived dataset[59].

`dumux-braindiffusion-miniapp`: A reuse example code that provides a simulator that uses the provided data set (C++ code, based on the DuMu^x/DUNE framework[60–62] and `GridFormat`[63]). The code is publicly available at `https://github.com/timokoch/dumux-braindiffusion-miniapp` and as an archived dataset[64] and may be helpful for users interested in using the provided data in a simulation reuse setup.

References

[1] Humberto Mestre, Jeffrey Tithof, Ting Du, Wei Song, Weiguo Peng, Amanda M. Sweeney, Genaro Olveda, John H. Thomas, Maiken Nedergaard, and Douglas H. Kelley. Flow of cerebrospinal fluid is driven by arterial pulsations and is reduced in hypertension. *Nature Communications*, 9:4878, November 2018. ISSN 2041-1723. doi:10.1038/s41467-018-07318-3. URL `https://www.ncbi.nlm.nih.gov/pmc/articles/PMC6242982/`.

[2] Vegard Vinje, Geir Ringstad, Erika Kristina Lindstrøm, Lars Magnus Valnes, Marie E. Rognes, Per Kristian Eide, and Kent-Andre Mardal. Respiratory influence on cerebrospinal fluid flow – a computational study based on long-term intracranial pressure measurements. *Scientific Reports*, 9(1), July 2019. ISSN 2045-2322. doi:10.1038/s41598-019-46055-5.

[3] Susanne J. van Veluw, Steven S. Hou, Maria Calvo-Rodriguez, Michal Arbel-Ornath, Austin C. Snyder, Matthew P. Frosch, Steven M. Greenberg, and Brian J. Bacskai. Vasomotion as a driving force for paravascular clearance in the awake mouse brain. *Neuron*, 105(3):549–561.e5, February 2020. ISSN 0896-6273. doi:10.1016/j.neuron.2019.10.033.

[4] Laura Bojarskaite, Alexandra Vallet, Daniel M. Bjørnstad, Kristin M. Gullestad Binder, Céline Cunen, Kjell Heuser, Miroslav Kuchta, Kent-Andre Mardal, and Rune Enger. Sleep cycle-dependent vascular dynamics in male mice and the predicted effects on perivascular cerebrospinal fluid flow and solute transport. *Nature Communications*, 14(1), February 2023. ISSN 2041-1723. doi:10.1038/s41467-023-36643-5.

[5] Jeffrey J. Iliff, Minghuan Wang, Yonghong Liao, Benjamin A. Plogg, Weiguo Peng, Georg A. Gundersen, Helene Benveniste, G. Edward Vates, Rashid Deane, Steven A. Goldman, Erlend A. Nagelhus, and Maiken Nedergaard. A paravascular pathway facilitates csf flow through the brain parenchyma and the clearance of interstitial solutes, including amyloid β. *Science Translational Medicine*, 4(147), 2012. ISSN 1946-6242. doi:10.1126/scitranslmed.3003748.

[6] Lulu Xie, Hongyi Kang, Qiwu Xu, Michael J. Chen, Yonghong Liao, Meenakshisundaram Thiyagarajan, John O'Donnell, Daniel J. Christensen, Charles Nicholson, Jeffrey J. Iliff, Takahiro Takano, Rashid Deane, and Maiken Nedergaard. Sleep drives metabolite clearance from the adult brain. *Science*, 342(6156):373–377, 2013. ISSN 1095-9203. doi:10.1126/science.1241224.

[7] Tomas Bohr, Poul G. Hjorth, Sebastian C. Holst, Sabina Hrabětová, Vesa Kiviniemi, Tuomas Lilius, Iben Lundgaard, Kent-Andre Mardal, Erik A. Martens, Yuki Mori, U. Valentin Nägerl, Charles Nicholson, Allen Tannenbaum, John H. Thomas, Jeffrey Tithof, Helene Benveniste, Jeffrey J. Iliff, Douglas H. Kelley, and Maiken Nedergaard. The glymphatic system: Current understanding and modeling. *iScience*, 25(9):104987, 2022. ISSN 2589-0042. doi:10.1016/j.isci.2022.104987.

[8] Ravi Teja Kedarasetti, Patrick J. Drew, and Francesco Costanzo. Arterial pulsations drive oscillatory flow of CSF but not directional pumping. *Scientific Reports*, 10(1), June 2020. doi:10.1038/s41598-020-66887-w.

[9] Francesco Romanò, Vinod Suresh, Peter A. Galie, and James B. Grotberg. Peristaltic flow in the glymphatic system. *Scientific Reports*, 10(1), December 2020. ISSN 2045-2322. doi:10.1038/s41598-020-77787-4.

[10] M. Keith Sharp. Pulsatile cerebral paraarterial flow by peristalsis, pressure and directional resistance. *Fluids and Barriers of the CNS*, 20(1), June 2023. ISSN 2045-8118. doi:10.1186/s12987-023-00445-0.

[11] Cécile Daversin-Catty, Vegard Vinje, Kent-André Mardal, and Marie E. Rognes. The mechanisms behind perivascular fluid flow. *PLOS ONE*, 15(12):e0244442, December 2020. doi:10.1371/journal.pone.0244442.

[12] Mahdi Asgari, Diane de Zélicourt, and Vartan Kurtcuoglu. Glymphatic solute transport does not require bulk flow. *Scientific Reports*, 6(1), December 2016. doi:10.1038/srep38635.

[13] Alex J. Smith and Alan S. Verkman. The "glymphatic" mechanism for solute clearance in alzheimer's disease: game changer or unproven speculation? *The FASEB Journal*, 32(2):543–551, January 2018. ISSN 1530-6860. doi:10.1096/fj.201700999.

[14] Alexandre Poulain, Jørgen Riseth, and Vegard Vinje. Multi-compartmental model of glymphatic clearance of solutes in brain tissue. *PLOS ONE*, 18(3):e0280501, March 2023. ISSN 1932-6203. doi:10.1371/journal.pone.0280501.

[15] Brett Tully and Yiannis Ventikos. Cerebral water transport using multiple-network poroelastic theory: Application to normal pressure hydrocephalus. *Journal of Fluid Mechanics*, 667:188–215, November 2010. doi:10.1017/s0022112010004428.

[16] Liwei Guo, John C. Vardakis, Dean Chou, and Yiannis Ventikos. A multiple-network poroelastic model for biological systems and application to subject-specific modelling of cerebral fluid transport. *International Journal of Engineering Science*, 147:103204, February 2020. doi:10.1016/j.ijengsci.2019.103204.

[17] Stephen B. Hladky and Margery A. Barrand. The glymphatic hypothesis: the theory and the evidence. *Fluids and Barriers of the CNS*, 19(1), 2022. ISSN 2045-8118. doi:10.1186/s12987-021-00282-z.

[18] E. Turgut Tali, Nil Ercan, Gaida Krumina, Mohammed Rudwan, Angel Mironov, Qing Yu Zeng, and J. Randy Jinkins. Intrathecal gadolinium (gadopentetate dimeglumine) enhanced magnetic resonance myelography and cisternography: Results of a multicenter study. *Investigative Radiology*, 37(3):152–159, 2002. ISSN 0020-9996. doi:10.1097/00004424-200203000-00008.

[19] L. J. Vanopdenbosch, P. Dedeken, J. W. Casselman, and S. A. P. A. Vlaminck. MRI with intrathecal gadolinium to detect a csf leak: a prospective open-label cohort study. *Journal of Neurology, Neurosurgery & Psychiatry*, 82(4):456–458, 2010. ISSN 0022-3050. doi:10.1136/jnnp.2009.180752.

[20] O. Algin and B. Turkbey. Intrathecal gadolinium-enhanced mr cisternography: A comprehensive review. *American Journal of Neuroradiology*, 34(1):14–22, 2012. ISSN 1936-959X. doi:10.3174/ajnr.a2899.

[21] Per Kristian Eide and Geir Ringstad. MRI with intrathecal MRI gadolinium contrast medium administration: a possible method to assess glymphatic function in human brain. *Acta Radiologica Open*, 4(11): 205846011560963, November 2015. ISSN 2058-4601. doi:10.1177/2058460115609635. URL `http://dx.doi.org/10.1177/2058460115609635`.

[22] Geir Ringstad, Svein Are Sirirud Vatnehol, and Per Kristian Eide. Glymphatic MRI in idiopathic normal pressure hydrocephalus. *Brain*, 140(10):2691–2705, 2017. ISSN 1460-2156. doi:10.1093/brain/awx191.

[23] Geir Ringstad, Lars M. Valnes, Anders M. Dale, Are H. Pripp, Svein-Are S. Vatnehol, Kyrre E. Emblem, Kent-Andre Mardal, and Per K. Eide. Brain-wide glymphatic enhancement and clearance in humans assessed with MRI. *JCI Insight*, 3(13), 2018. ISSN 2379-3708. doi:10.1172/jci.insight.121537.

[24] Per K Eide and Geir Ringstad. Delayed clearance of cerebrospinal fluid tracer from entorhinal cortex in idiopathic normal pressure hydrocephalus: A glymphatic magnetic resonance imaging study. *Journal of Cerebral Blood Flow & Metabolism*, 39(7):1355–1368, 2018. ISSN 1559-7016. doi:10.1177/0271678x18760974.

[25] C.S. Edeklev, M. Halvorsen, G. Løvland, S.A.S. Vatnehol, Ø. Gjertsen, B. Nedregaard, R. Sletteberg, G. Ringstad, and P.K. Eide. Intrathecal use of gadobutrol for glymphatic MR imaging: Prospective safety study of 100 patients. *American Journal of Neuroradiology*, 40(8):1257–1264, 2019. ISSN 1936-959X. doi:10.3174/ajnr.a6136.

[26] R. Watts, J.M. Steinklein, L. Waldman, X. Zhou, and C.G. Filippi. Measuring glymphatic flow in man using quantitative contrast-enhanced MRI. *American Journal of Neuroradiology*, 2019. ISSN 1936-959X. doi:10.3174/ajnr.a5931.

[27] Per Kristian Eide, Vegard Vinje, Are Hugo Pripp, Kent-Andre Mardal, and Geir Ringstad. Sleep deprivation impairs molecular clearance from the human brain. *Brain*, 144(3):863–874, 2021. ISSN 1460-2156. doi:10.1093/brain/awaa443.

[28] Per Kristian Eide, Aslan Lashkarivand, Åsmund Aleksander Hagen-Kersten, Øivind Gjertsen, Bård Nedregaard, Ruth Sletteberg, Grethe Løvland, Svein Are Sirirud Vatnehol, Are Hugo Pripp, Lars Magnus Valnes, and Geir Ringstad. Intrathecal contrast-enhanced magnetic resonance imaging of cerebrospinal fluid dynamics and glymphatic enhancement in idiopathic normal pressure hydrocephalus. *Frontiers in Neurology*, 13, 2022. ISSN 1664-2295. doi:10.3389/fneur.2022.857328.

[29] Matthias J. P. van Osch, Anders Wåhlin, Paul Scheyhing, Ingrid Mossige, Lydiane Hirschler, Anders Eklund, Klara Mogensen, Ryszard Gomolka, Alexander Radbruch, Sara Qvarlander, Andreas Decker, Maiken Nedergaard, Yuki Mori, Per Kristian Eide, Katerina Deike, and Geir Ringstad. Human brain clearance imaging: Pathways taken by magnetic resonance imaging contrast agents after administration in cerebrospinal fluid and blood. *NMR in Biomedicine*, 37(9), 2024. ISSN 1099-1492. doi:10.1002/nbm.5159.

[30] Merete Halvorsen, Camilla Sæthre Edeklev, Jorunn Fraser-Green, Grethe Løvland, Svein Are Sirirud Vatnehol, Øivind Gjertsen, Bård Nedregaard, Ruth Sletteberg, Geir Ringstad, and Per Kristian Eide. Off-label intrathecal use of gadobutrol: safety study and comparison of administration protocols. *Neuroradiology*, 63(1):51–61, 2020. ISSN 1432-1920. doi:10.1007/s00234-020-02519-4.

[31] Mihilkumar Patel, Almohannad Atyani, Jean-Paul Salameh, Matthew McInnes, and Santanu Chakraborty. Safety of intrathecal administration of gadolinium-based contrast agents: A systematic review and meta-analysis. *Radiology*, 297(1):75–83, October 2020. ISSN 1527-1315. doi:10.1148/radiol.2020191373.

[32] Geir Ringstad and Per Kristian Eide. Safety of intrathecal gadolinium-based contrast agents and benefit versus risk. *Radiology*, 299(1):E223–E224, April 2021. ISSN 1527-1315. doi:10.1148/radiol.2021203351.

[33] Per Kristian Eide, Are Hugo Pripp, Geir Ringstad, and Lars Magnus Valnes. Impaired glymphatic function in idiopathic intracranial hypertension. *Brain Communications*, 3(2), 2021. ISSN 2632-1297. doi:10.1093/braincomms/fcab043.

[34] Per K Eide, Espen Mariussen, Hilde Uggerud, Are H Pripp, Aslan Lashkarivand, Bjørnar Hassel, Hege Christensen, Markus Herberg Hovd, and Geir Ringstad. Clinical application of intrathecal gadobutrol for assessment of cerebrospinal fluid tracer clearance to blood. *JCI insight*, 6(9):e147063, 2021. doi:10.1172/jci.insight.147063.

[35] Tryggve Holck Storås, Sofie Lysholm Lian, Ingrid Mossige, Jørgen Riseth, Siri Fløgstad Svensson, Grethe Løvland, Geir Ringstad, Kent-André Mardal, Kyrre Eeg Emblem, and Kaja Nordengen. <scp>t2</scp> -weighted <scp>t1</scp> mapping and automated segmentation of <scp>csf</scp>: Assessment of solute gradients in the healthy brain. *Journal of Magnetic Resonance Imaging*, November 2025. ISSN 1522-2586. doi:10.1002/jmri.70169.

[36] Xiangrui Li, Paul S. Morgan, John Ashburner, Jolinda Smith, and Christopher Rorden. The first step for neuroimaging data analysis: DICOM to NIfTI conversion. *Journal of Neuroscience Methods*, 264:47–56, May 2016. ISSN 1872-678X. doi:10.1016/j.jneumeth.2016.03.001.

[37] D. C. Look and D. R. Locker. Time Saving in Measurement of NMR and EPR Relaxation Times. *Review of Scientific Instruments*, 41(2):250–251, February 1970. ISSN 0034-6748. doi:10.1063/1.1684482.

[38] Glenn S Slavin. On the use of the "Look-Locker correction" for calculating T1 values from MOLLI. *Journal of Cardiovascular Magnetic Resonance*, 16(Suppl 1):P55, January 2014. ISSN 1097-6647. doi:10.1186/1532-429X-16-S1-P55. URL `https://www.ncbi.nlm.nih.gov/pmc/articles/PMC4044058/`.

[39] Pauli Virtanen, Ralf Gommers, Travis E. Oliphant, Matt Haberland, Tyler Reddy, David Cournapeau, Evgeni Burovski, Pearu Peterson, Warren Weckesser, Jonathan Bright, Stéfan J. van der Walt, Matthew Brett, Joshua Wilson, K. Jarrod Millman, Nikolay Mayorov, Andrew R. J. Nelson, Eric Jones, Robert Kern, Eric Larson, C J Carey, İlhan Polat, Yu Feng, Eric W. Moore, Jake VanderPlas, Denis Laxalde, Josef Perktold, Robert Cimrman, Ian Henriksen, E. A. Quintero, Charles R. Harris, Anne M. Archibald, Antônio H. Ribeiro, Fabian Pedregosa, Paul van Mulbregt, and SciPy 1.0 Contributors. SciPy 1.0: Fundamental Algorithms for Scientific Computing in Python. *Nature Methods*, 17:261–272, 2020. doi:10.1038/s41592-019-0686-2.

[40] J. J. E. in den Kleef and J. J. M. Cuppen. RLSQ: T1, T2, and ρ calculations, combining ratios and least squares. *Magnetic Resonance in Medicine*, 5(6):513–524, 1987. ISSN 1522-2594. doi:10.1002/mrm.1910050602. URL `https://onlinelibrary.wiley.com/doi/abs/10.1002/mrm.1910050602`.

[41] Jui-Cheng Yen, Fu-Juay Chang, and Shyang Chang. A new criterion for automatic multilevel thresholding. *IEEE Transactions on Image Processing*, 4(3):370–378, March 1995. ISSN 1941-0042. doi:10.1109/83.366472. URL `https://ieeexplore.ieee.org/document/366472`.

[42] Long Xie, Laura E. M. Wisse, John Pluta, Robin de Flores, Virgine Piskin, Jose V. Manjón, Hongzhi Wang, Sandhitsu R. Das, Song-Lin Ding, David A. Wolk, and Paul A. Yushkevich. Automated segmentation of medial temporal lobe subregions on in vivo T1-weighted MRI in early stages of Alzheimer's disease. *Human Brain Mapping*, 40(12):3431–3451, April 2019. ISSN 1065-9471. doi:10.1002/hbm.24607. URL `https://www.ncbi.nlm.nih.gov/pmc/articles/PMC6697377/`.

[43] Martin Rohrer, Hans Bauer, Jan Mintorovitch, Martin Requardt, and Hanns-Joachim Weinmann. Comparison of magnetic properties of MRI contrast media solutions at different magnetic field strengths. *Investigative Radiology*, 40(11):715–724, November 2005. ISSN 0020-9996. doi:10.1097/01.rli.0000184756.66360.d3.

[44] Mark Jenkinson, Christian F. Beckmann, Timothy E.J. Behrens, Mark W. Woolrich, and Stephen M. Smith. Fsl. *NeuroImage*, 62(2):782–790, August 2012. ISSN 1053-8119. doi:10.1016/j.neuroimage.2011.09.015.

[45] Jesper L.R. Andersson, Stefan Skare, and John Ashburner. How to correct susceptibility distortions in spin-echo echo-planar images: application to diffusion tensor imaging. *NeuroImage*, 20(2):870–888, 2003. ISSN 1053-8119. doi:10.1016/s1053-8119(03)00336-7.

[46] Stephen M. Smith, Mark Jenkinson, Mark W. Woolrich, Christian F. Beckmann, Timothy E.J. Behrens, Heidi Johansen-Berg, Peter R. Bannister, Marilena De Luca, Ivana Drobnjak, David E. Flitney, Rami K. Niazy, James Saunders, John Vickers, Yongyue Zhang, Nicola De Stefano, J. Michael Brady, and Paul M. Matthews. Advances in functional and structural mr image analysis and implementation as fsl. *NeuroImage*, 23:S208–S219, 2004. ISSN 1053-8119. doi:10.1016/j.neuroimage.2004.07.051.

[47] Jesper L.R. Andersson and Stamatios N. Sotiropoulos. An integrated approach to correction for off-resonance effects and subject movement in diffusion mr imaging. *NeuroImage*, 125:1063–1078, 2016. ISSN 1053-8119. doi:10.1016/j.neuroimage.2015.10.019.

[48] Kent-André Mardal, Marie E. Rognes, Travis B. Thompson, and Lars Magnus Valnes. *Mathematical Modeling of the Human Brain: From Magnetic Resonance Images to Finite Element Simulation*. Springer International Publishing, 2022. ISBN 9783030951368. doi:10.1007/978-3-030-95136-8.

[49] R. Watts, J.M. Steinklein, L. Waldman, X. Zhou, and C.G. Filippi. Measuring glymphatic flow in man using quantitative contrast-enhanced MRI. *American Journal of Neuroradiology*, 2019. ISSN 1936-959X. doi:10.3174/ajnr.a5931.

[50] Bastian Zapf, Lars Magnus Valnes, Kent-Andre Mardal, and Ludmil Zikatanov. Quantifying cerebrospinal fluid tracer concentration in the brain. In Jørgen Dokken, Kent-Andre Mardal, Lars Magnus Rognes, Marie E Valnes, and Vegard Vinje, editors, *MRI2FEM II: from magnetic resonance images to computational brain mechanics*. Springer, 2025. ISBN 978-3-032-00679-0.

[51] Bruce Fischl. FreeSurfer. *NeuroImage*, 62(2):774–781, August 2012. ISSN 1095-9572. doi:10.1016/j.neuroimage.2012.01.021.

[52] Leonie Henschel, Sailesh Conjeti, Santiago Estrada, Kersten Diers, Bruce Fischl, and Martin Reuter. Fastsurfer-a fast and accurate deep learning based neuroimaging pipeline. *NeuroImage*, 219:117012, 2020. doi:10.1016/j.neuroimage.2020.117012.

[53] C. Sullivan and Alexander Kaszynski. Pyvista: 3d plotting and mesh analysis through a streamlined interface for the visualization toolkit (vtk). *Journal of Open Source Software*, 4(37):1450, 2019. ISSN 2475-9066. doi:10.21105/joss.01450.

[54] Jørgen Riseth, Timo Koch, Sofie Lian, Tryggve Storås, Ludmil T. Zikatanov, Lars Magnus Valnes, Kaja Nordengen, and Kent-Andre Mardal. The gonzo dataset: Human brain mri data of csf tracer evolution over 72h for data-integrated simulations, July 2025. URL `https://doi.org/10.5281/zenodo.14266867`.

[55] A.F. Stalder, D. v. Elverfeldt, D. Paul, J. Hennig, and M. Markl. Variable echo time imaging: Signal characteristics of 1-m gadobutrol contrast agent at 1.5 and 3t. *Magnetic Resonance in Medicine*, 59(1):113–123, December 2007. ISSN 1522-2594. doi:10.1002/mrm.21345.

[56] Conrad E Johanson, John A Duncan, Petra M Klinge, Thomas Brinker, Edward G Stopa, and Gerald D Silverberg. Multiplicity of cerebrospinal fluid functions: New challenges in health and disease. *Cerebrospinal Fluid Research*, 5(1), May 2008. ISSN 1743-8454. doi:10.1186/1743-8454-5-10.

[57] Yaqi Shen, Frank L. Goerner, Christopher Snyder, John N. Morelli, Dapeng Hao, Daoyu Hu, Xiaoming Li, and Val M. Runge. T1 relaxivities of gadolinium-based magnetic resonance contrast agents in human whole blood at 1.5, 3, and 7 t. *Investigative Radiology*, 50(5):330–338, May 2015. ISSN 0020-9996. doi:10.1097/rli.0000000000000132.

[58] Jørgen Riseth and Timo Koch. Gonzo processing pipeline, v1.0.0, November 2025. URL `https://doi.org/10.5281/zenodo.17760932`.

[59] Jørgen Riseth. gmri2fem, v0.2.8, August 2025. URL `https://doi.org/10.5281/zenodo.16677013`.

[60] Timo Koch, Dennis Gläser, Kilian Weishaupt, et al. Dumu^{x} 3 - an open-source simulator for solving flow and transport problems in porous media with a focus on model coupling. *Computers & Mathematics with Applications*, 2021. ISSN 0898-1221. doi:10.1016/j.camwa.2020.02.012.

[61] Peter Bastian, Markus Blatt, Andreas Dedner, Nils-Arne Dreier, Christian Engwer, René Fritze, Carsten Gräser, Christoph Grüninger, Dominic Kempf, Robert Klöfkorn, Mario Ohlberger, and Oliver Sander. The Dune framework: Basic concepts and recent developments. *Computers & Mathematics with Applications*, 81: 75–112, 2021. ISSN 0898-1221. doi:10.1016/j.camwa.2020.06.007.

[62] Martin Alkämper, Andreas Dedner, Robert Klöfkorn, and Martin Nolte. The dune-alugrid module. *Archive of Numerical Software*, Vol 4, 2016. doi:10.11588/ANS.2016.1.23252.

[63] Dennis Gläser, Timo Koch, and Bernd Flemisch. GridFormat: header-only C++-library for grid file I/O. *Journal of Open Source Software*, 8(90):5778, 2023. ISSN 2475-9066. doi:10.21105/joss.05778.

[64] Timo Koch and Jørgen Riseth. Software for reuse example in: MRI data of CSF tracer evolution over 72h in human brain for data-integrated simulations", 2025.

[65] Lin Chen, M Bernstein, J Huston, and S Fain. Measurements of T1 relaxation times at 3.0 T: implications for clinical MRA. In *Proceedings of the 9th Annual Meeting of ISMRM, Glasgow, Scotland*, volume 1391, 2001.

[66] Hanzhang Lu, Lidia M. Nagae-Poetscher, Xavier Golay, Doris Lin, Martin Pomper, and Peter C.M. van Zijl. Routine clinical brain MRI sequences for use at 3.0 Tesla. *Journal of Magnetic Resonance Imaging*, 22(1): 13–22, 2005. ISSN 1522-2586. doi:10.1002/jmri.20356.

[67] Wanyong Shin, Hong Gu, and Yihong Yang. Fast high-resolution T1 mapping using inversion-recovery look-locker echo-planar imaging at steady state: Optimization for accuracy and reliability. *Magnetic Resonance in Medicine*, 61(4):899–906, 2009. ISSN 1522-2594. doi:10.1002/mrm.21836. URL `https://onlinelibrary.wiley.com/doi/abs/10.1002/mrm.21836`.

[68] Matthias A. Dieringer, Michael Deimling, Davide Santoro, Jens Wuerfel, Vince I. Madai, Jan Sobesky, Florian von Knobelsdorff-Brenkenhoff, Jeanette Schulz-Menger, and Thoralf Niendorf. Rapid Parametric Mapping of the Longitudinal Relaxation Time T1 Using Two-Dimensional Variable Flip Angle Magnetic Resonance Imaging at 1.5 Tesla, 3 Tesla, and 7 Tesla. *PLOS ONE*, 9(3):e91318, March 2014. ISSN 1932-6203. doi:10.1371/journal.pone.0091318. URL `https://journals.plos.org/plosone/article?id=10.1371/journal.pone.0091318`.

[69] P. J. Wright, O. E. Mougin, J. J. Totman, A. M. Peters, M. J. Brookes, R. Coxon, P. E. Morris, M. Clemence, S. T. Francis, R. W. Bowtell, and P. A. Gowland. Water proton T1 measurements in brain tissue at 7, 3, and 1.5T using IR-EPI, IR-TSE, and MPRAGE: results and optimization. *Magnetic Resonance Materials in Physics, Biology and Medicine*, 21(1):121, February 2008. ISSN 1352-8661. doi:10.1007/s10334-008-0104-8. URL `https://doi.org/10.1007/s10334-008-0104-8`.

[70] Johanna Helenius, Lauri Soinne, Jussi Perkiö, Oili Salonen, Aki Kangasmäki, Markku Kaste, Richard AD Carano, Hannu J Aronen, and Turgut Tatlisumak. Diffusion-weighted MR imaging in normal human brains in various age groups. *American journal of neuroradiology*, 23(2):194–199, 2002.

[71] Vegard Vinje, Bastian Zapf, Geir Ringstad, Per Kristian Eide, Marie E. Rognes, and Kent-Andre Mardal. Human brain solute transport quantified by glymphatic MRI-informed biophysics during sleep and sleep deprivation. *Fluids and Barriers of the CNS*, 20(1), 2023. ISSN 2045-8118. doi:10.1186/s12987-023-00459-8.

[72] Luminita Moraru and Lucian Dimitrievici. Apparent diffusion coefficient of the normal human brain for various experimental conditions. In *AIP Conference Proceedings*, volume 1792, page 040005. Author(s), 2017. doi:10.1063/1.4972383.

[73] P. Mukherjee, J.I. Berman, S.W. Chung, C.P. Hess, and R.G. Henry. Diffusion tensor MR imaging and fiber tractography: Theoretic underpinnings. *American Journal of Neuroradiology*, 29(4):632–641, March 2008. ISSN 1936-959X. doi:10.3174/ajnr.a1051.

[74] R.N. Sener. Diffusion MRI: apparent diffusion coefficient (ADC) values in the normal brain and a classification of brain disorders based on ADC values. *Computerized Medical Imaging and Graphics*, 25(4):299–326, July 2001. ISSN 0895-6111. doi:10.1016/s0895-6111(00)00083-5.

Author contributions statement

J.R.: Data curation, Formal analysis, Investigation, Methodology, Software, Validation, Visualization, Writing – original draft; T.K.: Formal analysis, Investigation, Software, Methodology, Supervision, Validation, Visualization, Writing – original draft; S.L.: Data curation, Methodology, Investigation, Writing – review & editing; T.H.S.: Data curation, Formal analysis, Methodology, Writing – review & editing; L.M.V.: Software, Methodology, Writing – review & editing; L.Z.: Conceptualization, Investigation, Writing – review & editing; K.N.: Conceptualization, Funding acquisition, Methodology, Project Administration, Supervision, Writing – review & editing; K.A.M.: Conceptualization, Methodology, Funding acquisition, Project Administration, Supervision, Writing – original draft;

Competing interests

The authors have no competing interests.

Acknowledgements

The authors thank Geir Ringstadt and Per-Kristian Eide for spearheading the development of glymphatic MRI and for fruitful discussions. The authors are grateful to the anonymous volunteer for participating in the study and giving informed consent to open publication, allowing us to disseminate this unique data set.

S.L. and K.N. acknowledge funding from the South Eastern Norway Health Authority (Helse Sør-Øst) within project 2022022 (Clearance pathways in Parkinson's disease) and the Norwegian Health Association (Nasjonalforeningen for folkehelsen) within projects 25598 and 28398. T.K. acknowledges funding from the European Union's Horizon 2020 Research and Innovation programme under the Marie Skłodowska-Curie Actions Grant agreement No 801133 (Scientia fellows II). T.K. and K.A.M. acknowledge funding by the Research Council of Norway, project 301013 (Alzheimer's physics). T.K., J.N.R and K.A.M. acknowledge funding by the European Research Council under grant 101141807 (aCleanBrain). K.A.M. and L.M.V acknowledges the funding from the "Computational Hydrology project" a strategic Sustainability initiative at the Faculty of Natural Sciences, UiO. K.A.M. acknowledges funding from the Stiftelsen Kristian Gerhard Jebsen via the K. G. Jebsen Centre for Brain Fluid Research and the national infrastructure for computational science in Norway, Sigma2, via grant NN9279K. The work of L.T.Z. was supported in part by U.S. NSF DMS-220829 and the U.S.-Norway Fulbright Foundation.

Table 1: Summary of different file formats included in the data record, with a description of their purpose and a path describing either a directory or the full path of an example file of the corresponding file format.

Filetype	Description
`.tsv`	Textfile for table-formatted data related to MRI-images, such as a time of acquisition for each sequence relative to time of contrast injection. May be opened with any text editor, or in spreadsheet software. **Example path:** `mri_dataset/timetable.tsv`
`.csv`	Textfile for table-formatted data of interest, such as tracer concentration measurements in blood plasma. May be opened with any text editor, or in spreadsheet software. **Example path:** `mri_dataset/blood_concentrations.csv`
`.nii.gz`	Primary format for MRI data (raw, derivative, processed, T1-maps, concentration maps, segmentations) in NIfTI-1. Opens in most software for viewing MRI, such as FreeSurfer's Freeview, but have to be unzipped before opening in some viewers. **Example directory:** `mri_dataset/sub-01/ses-XX/anat/`
`.json`	Accompanying metadata for MRI images (BIDS sidecar-file). Opens in any text editor. **Example directory:** `mri_dataset/sub-01/ses-XX/anat/`
`.bval`	Plaintext file with gradient field strengths for diffusion-weighted imaging (DWI). Opens in any text editor. **Example directory:** `mri_dataset/sub-01/ses-01/dwi/`
`.bvec`	Plaintext file with gradient vectors for diffusion-weighted imaging (DWI). Opens in any text editor. **Example directory:** `mri_dataset/sub-01/ses-01/dwi/`
`.mgz`	The FreeSurfer `.mgz` format is a compressed version of the FreeSurfer `.mgh` format, which is used to store MRI-data. Compression is conducted using Zlib. Opens in FreeSurfer's Freeview, and some other MRI viewers, but may have to be converted to NIfTI for other software such as FSLEyes. **Example directory:** `mri_processed_data/fastsurfer/sub-01`
`.mat`	Affine transformation matrix in plaintext format, used to reslice images. Opens in any text editor. **Example directory:** `mri_processed_data/sub-01/transforms/`
`.stl`	STL-format surfaces used as input for 3D mesh generation. Opens in, for example, Paraview. **Example directory:** `mri_processed_data/sub-01/modeling/surfaces/`
`.hdf`	3D tetrahedral mesh and mapped MRI data (HDF5, FEniCS-compatible). Contents may be inspected with e.g. h5ls, but is structured for reading in python scripts with FEniCS. **Example directory:** `mri_processed_data/sub-01/modeling/resolution32/`
`.vtu`	3D tetrahedral mesh and mapped MRI data (VTK Unstructured grid). Opens in Paraview or other VTK-compatible 3D visualization software. **Example directory:** `mri_processed_data/sub-01/modeling/resolution32/`
`.xdmf`	Mesh data file (XDMF3) containing facet-tags (boundaries) from the meshing process. Opens in Paraview, or may be read with python scripts with FEniCS. **Example directory:** `mri_processed_data/sub-01/modeling/resolution32/mesh_xdmfs/`
`.h5`	Data file associated with XDMF mesh data (HDF5 format). Not intended for reading directly; but is use by software which opens the accompanying xdmf-file. **Example directory:** `mri_processed_data/sub-01/modeling/resolution32/mesh_xdmfs/`

Table 2: Total tracer amount measured within brain tissue and in the CSF-filled spaces surrounding the brain, as indicated by Fig. 12.

	Tracer amount ($\times 10^{-2}$ mmol)		
Time (hours)	Brain+CSF	Brain	CSF
4	7.85	1.64	6.16
24	11.8	5.19	6.57
48	8.59	4.53	4.02
70	5.06	2.93	2.12

Table 3: T_1 longitudinal relaxation times and apparent diffusion coefficient (ADC) values as reported by various sources for cerebrospinal fluid, gray matter, and white matter, compared to the values obtained in this study.

	cerebrospinal fluid	gray matter	white matter	reference
T_1 in ms (mean ± std.)	4465 ± 154	1622 ± 558	955 ± 180	This study
	416 ± 263	1445 ± 119	791 ± 27	[65]
	3817 ± 424	1135 ± 79	732 ± 56	[66]*
	4391 ± 545	1460 ± 33	943 ± 57	[67]
	-	1615 ± 149	911 ± 15	[68]
	-	1600 ± 110	840 ± 50	[69]
ADC in $1 \times 10^{-9}\,\mathrm{m\,s^{-2}}$ (mean ± std.)	-	1.05 ± 0.17	0.77 ± 0.17	This study
	-	0.89 ± 0.04	0.75 ± 0.03	[70]
	-	0.92 ± 0.02	0.87 ± 0.02	[71]
	-	0.681 ± 0.07	0.613 ± 0.07	[72]
	-	0.67–0.83	0.84 ± 0.11	[73]
	-	-	0.84 ± 0.11	[74]

∗ White matter and gray matter values are averaged over smaller reference regions used in the article.

Table 4: Molar concentration of gadobutrol in blood plasma, c_P, in $\mathrm{mmol\,L^{-1}}$ using a direct sampling method. Reported acquisition time t is in minutes/hours relative to the injection time $t = 0\,\mathrm{min}$.

t	100/1.67	220/3.67	380/4.67	525/8.75	750/12.50	1230/20.50	1515/25.25	2430/40.50	2860/47.67
c_P	2.74E-04	4.37E-04	1.55E-03	2.07E-03	2.14E-03	2.20E-03	1.28E-03	2.31E-03	5.67E-04

Table 5: MRI sequence parameters used for the acquisition of T_1-weighted images (T1w), T_2-weighted images (T2w), diffusion tensor images (DTI), FLAIR, Look-locker (LL), and Mixed spin-echo inversion recovery (Mixed) images.

Sequence	T1w	T2w	DTI	FLAIR	LL	Mixed
Orientation	Sagittal	Sagittal	Transverse	Sagittal	Sagittal	Sagittal
Field of view (APxFHxRL)	256x256x184	256x256x184	240x240x125	250x250x182.5	256x256x184	224x224x180
Sampled voxel size (mm)	1x1x1	0.7x0.7x0.7	2.5x2.5x2.5	1x1x1	1x1x1	1x1x1
Reconstr. voxel size (mm)	0.5x0.5x0.5	0.33x0.33x0.35	2.5x2.5x2.5	0.49x0.49x0.5	1x1x1	0.5x0.5x0.5
Repetition time (ms)	5.2	3200	12200	4800	7.6	8350 / 11000
Inversion time	853	–	–	1650	–	2650
Flip angle (/refocus angle)	8	90/160	90	90/40	5	90/180
Echo time	2.3	565	60	340	3.5	700
Turbo factor	232	–	–	–	25	–
TSE-factor	–	105	–	167	–	166
Shot interval	3000	–	–	–	6000	–
Number of samplings	1	1	1	2	1	1
Bandwidth (Hz/pixel)	394	254	31.5	719	217	286
Compr. Sense accel.	2	6.3	–	8	25	9
Scan duration (min:sec)	4:10	6:30	7:15	4:34	12:17	7:44

Table 6: Error propagation analysis for the Look-Locker sequence concentration map reconstruction. Various statistics on the relative error $\mathrm{e} = \frac{||c_{\mathrm{est}} - c_{\mathrm{true}}||}{0.3} \times 100$ with a simulated signal to noise ratio (SNR) of 25 for different concentration ranges.

c in mmol/l	$0.00 - 0.05$	$0.05 - 0.10$	$0.10 - 0.15$	$0.15 - 0.20$	$0.20 - 0.25$	$0.25 - 0.30$
mean(e)	4.78	3.31	1.31	0.91	1.06	1.32
stddev(e)	3.45	1.92	1.01	0.71	0.79	0.99
5th(e)	0.69	0.94	0.17	0.09	0.10	0.14
median(e)	4.14	2.86	1.06	0.76	0.90	1.11
95th(e)	10.94	6.59	3.17	2.25	2.49	3.17
min(e)	0.20	0.44	0.06	0.02	0.03	0.04
max(e)	14.05	7.82	4.10	3.09	3.34	4.20

Table 7: Error propagation analysis for the Mixed sequence concentration map reconstruction. Various statistics on the relative error $\mathrm{e} = \frac{||c_{\mathrm{est}} - c_{\mathrm{true}}||}{0.3} \times 100$ with a simulated signal to noise ratio (SNR) of 25 for different concentration ranges.

c in mmol/l	$0.00 - 0.05$	$0.05 - 0.10$	$0.10 - 0.15$	$0.15 - 0.20$	$0.20 - 0.25$	$0.25 - 0.30$
mean(e)	2.09	2.98	4.58	6.85	10.15	14.54
stddev(e)	1.45	1.94	2.83	4.20	5.95	8.24
5th(e)	0.24	0.37	0.64	0.86	1.59	2.23
median(e)	1.86	2.74	4.35	6.52	9.80	14.29
95th(e)	4.67	6.32	9.51	13.91	20.00	27.68
min(e)	0.06	0.11	0.18	0.25	0.52	0.69
max(e)	5.91	7.89	11.58	17.21	24.50	33.61

Table 8: Error propagation analysis for the Look-Locker sequence T_1 map reconstruction. Various statistics on the relative error $e = \frac{||T_{1\text{est}} - T_{1\text{true}}||}{4.0} \times 100$ with a simulated signal to noise ratio (SNR) of 25 for different T_1 ranges.

T_1 in s	$0.5 - 1.0$	$1.0 - 1.5$	$1.5 - 2.0$	$2.0 - 2.5$	$2.5 - 3.0$	$3.0 - 3.5$	$3.5 - 4.0$	$4.0 - 4.5$
mean(e)	0.26	0.34	1.00	4.09	11.07	17.18	14.26	21.87
stddev(e)	0.20	0.27	0.82	2.24	11.87	15.22	15.12	21.88
5th(e)	0.03	0.03	0.12	1.00	2.91	1.51	0.96	1.88
median(e)	0.22	0.28	0.74	3.74	7.76	12.06	9.67	14.24
95th(e)	0.63	0.87	2.54	7.57	32.03	45.98	43.99	67.46
min(e)	0.01	0.01	0.04	0.37	1.41	0.44	0.19	0.60
max(e)	0.84	1.16	3.24	8.62	54.63	63.24	71.81	98.31

Table 9: Error propagation analysis for the Mixed sequence T_1 map reconstruction. Various statistics on the relative error $e = \frac{||T_{1\text{est}} - T_{1\text{true}}||}{4.0} \times 100$ with a simulated signal to noise ratio (SNR) of 25 for different T_1 ranges.

T_1 in s	$0.5 - 1.0$	$1.0 - 1.5$	$1.5 - 2.0$	$2.0 - 2.5$	$2.5 - 3.0$	$3.0 - 3.5$	$3.5 - 4.0$	$4.0 - 4.5$
mean(e)	3.37	3.06	3.20	3.75	4.62	5.55	7.19	8.18
stddev(e)	2.13	2.01	2.19	2.57	3.38	4.24	5.37	6.20
5th(e)	0.45	0.38	0.38	0.46	0.47	0.59	0.73	0.99
median(e)	3.14	2.80	2.87	3.34	4.00	4.57	6.17	6.71
95th(e)	7.07	6.60	7.14	8.22	10.79	13.37	16.87	19.94
min(e)	0.14	0.11	0.12	0.14	0.11	0.17	0.19	0.38
max(e)	8.51	8.44	9.06	10.87	14.16	17.45	22.75	25.94

Figure 2: **Pre-constrast MRI data.** Pre-contrast T_1-weighted, T_2-weighted, and FLAIR images are used for segmentation and cortical reconstruction: the T_1-weighted and FLAIR images by FreeSurfer's `recon-all`; the T_2-weighted image to create a CSF mask. *The individual depicted has provided written consent for inclusion of these images in this manuscript.*

Figure 3: **Look-Locker T_1 estimation.** **(a)** Sequence of Look-Locker images, representing the magnitude of the longitudinal magnetization at different times following an inverting pulse. **(b)** Look-Locker sequence's signal intensity in three example voxels from different regions, together with the fitted curves on the form 2. The signal intensities do not have a physically meaningful unit, and the y-axis is therefore unlabeled. *The individual depicted has provided written consent for inclusion of these images in this manuscript.*

Figure 4: T_1 **and concentration maps.** First two rows shows T_1 maps estimated from the Look-Locker and Mixed sequence. Third row shows the combined (Look-Locker / Mixed) T_1 maps, which is used to compute the concentration map in the final row.

Figure 5: **Diffusion tensor imaging.** DTI data represented by mean diffusivity (left), fractional anisotropy (right), and directionally coded fractional anisotropy (middle) with red in the (R)ight-(L)eft direction, green along the (A)nterior-(P)osterior and blue along the (S)uperior-(I)nferior axis.

Figure 6: **T_1-weighted images.** T_1-weighted images before normalization, pre-contrast and post-contrast injection at times 4 h, 24 h, 48 h and 70 h, ordered chronologically from left to right. *The individual depicted has provided written consent for inclusion of these images in this manuscript.*

figures/figure7.pdf

Figure 7: **Normalization of T_1-weighted images.** An illustration of the automated mask generation routine for the reference region: **(a)** The red lines represent planes along each coordinate axis. They intersect at a point close to the left orbital fat. The contours surrounding the points represent a Gaussian distribution centered at the intersecting point. **(b)** The left part shows the product between the Gaussian distribution from (a) and the T_1-weighted image, leaving an image consisting mainly of the orbital fat. A mask is generated from the corresponding image for each session. The masks from each session are intersected to create the reference region, shown in yellow on the right image. *The individual depicted has provided written consent for inclusion of these images in this manuscript.*

Figure 8: **Meshes and subdomain tags. (a)** top and bottom view of the brain mesh with edges to highlight each of the cells. **(b)** cell tags defining subdomains based on the enclosing surfaces during mesh generation. Cortical gray matter is dark gray, sub-cortical gray is light gray, and white matter is white. **(c)** ventricle surface mesh. **(d-f)** subdomain tags created by mapping the FreeSurfer MRI segmentation `aparc+aseg` in different views.

Figure 9: **CSF tracer concentration mapped onto brain surface.** Concentration shown in the range $0.0\,\mathrm{mmol\,L^{-1}}$ to $0.4\,\mathrm{mmol\,L^{-1}}$ as given by a piece-wise linear function mapped onto the surface of the brain mesh.

Figure 10: **Comparison to different T_1 analysis software. (a)** Scatterplot of our estimated T_1 vs. nICE T_1 for intracranial voxels. Estimated T_1 time vs. the T_1 time of the nICE-analysis from the pre-contrast Look-Locker sequence. **(a, inset)**: Empirical cumulative distribution (ECDF) of the absolute relative percentage difference (RPD) between our T_1-estimates and nICE-estimates for each of the sessions (log-scale). Absolute RPD is defined as $100 \times |(T_1 - T_1^{\mathrm{nICE}})/(0.5T_1 + 0.5T_1^{\mathrm{nICE}})|$ **(b)** Estimated T_1 time vs. the scanner-generated T_1 time from the first post-contrast Mixed sequence. The scanner's intensity cut-off causes the deviation for large T_1 values and is the reason for using our custom algorithm.

Figure 11: **LL/Mixed T_1 and concentration estimation: sensitivity to noise. (a)** Estimated versus true T_1 and concentration values when propagating noisy data through the estimation pipeline. Increasing concentration values correspond to decreasing T_1 times. The relationship is nonlinear, Eq. (7). The dashed line marks a chosen threshold value of the concentration (and corresponding T_1 time). Above the threshold, concentration estimates with the Look-Locker sequence appear more accurate than estimates with the Mixed sequence (and vice versa below the threshold). The figure is obtained with the script `noise/plot_noise_combined.py` (Code availability). **(b)** Scatterplot of the median T_1 estimates from Look-Locker compared to the median T_1 estimates from Mixed within different CSF regions. The size of the markers reflects the number of voxels in the given region. CSF regions are defined by a nearest neighbour interpolation of the FreeSurfer segmentation `aseg+aparc` onto the CSF mask.

Figure 12: **Estimated amount of tracer in the brain.** Graph of the the estimated total tracer amount in the CSF, the brain-tissue and the two combined, at each of the sessions. The different regions are illustrated in the right figure, with the brain in gray and CSF in blue. *The individual depicted has provided written consent for inclusion of these images in this manuscript.*

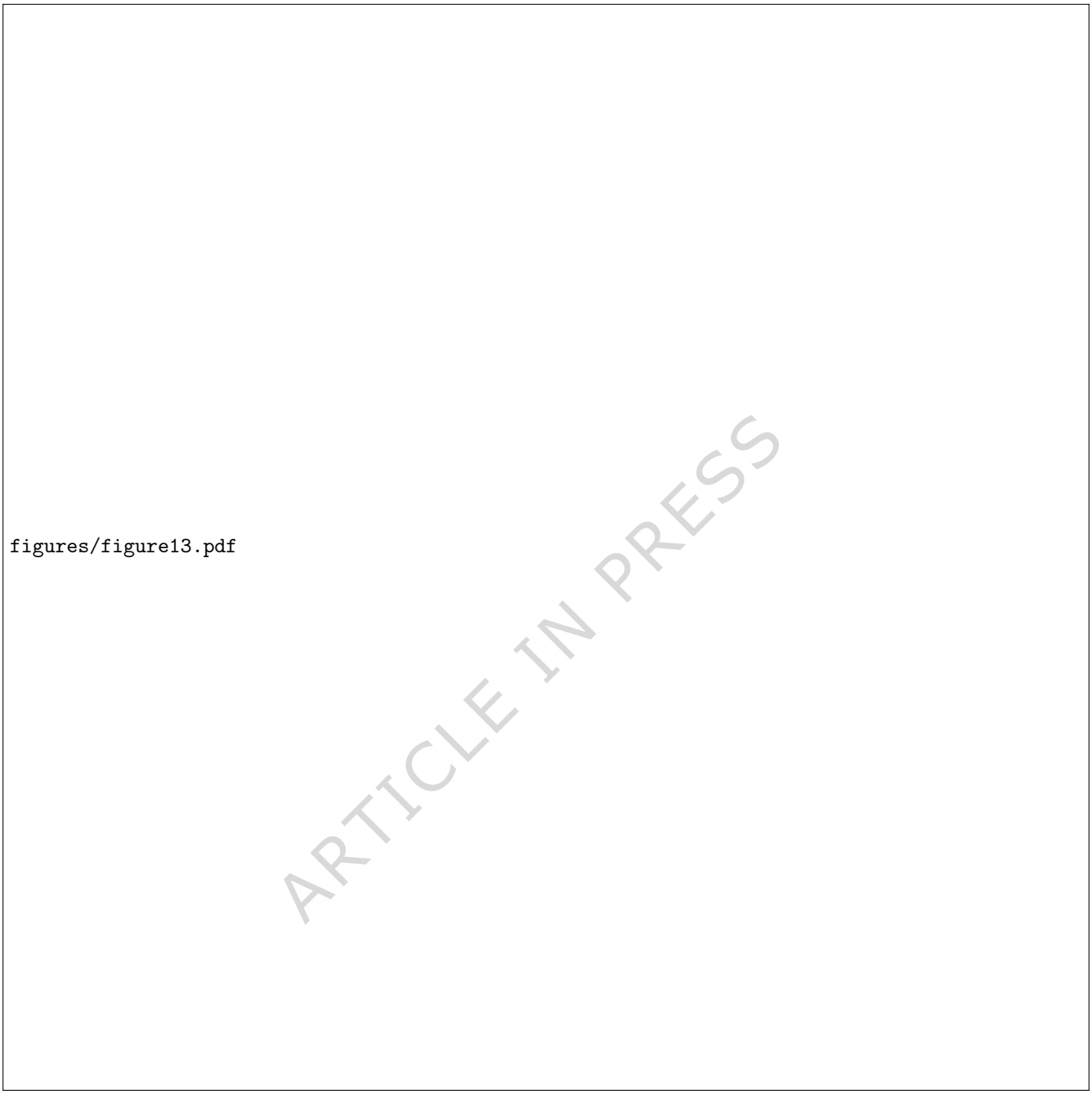

Figure 13: **Upper left:** Visualization of the error introduced by mapping the concentration data at 24 hours from the Cartesian MRI data grid in clinical resolution to the 3D volume mesh and back to the MR image grid. The leftmost panel shows the concentration data after mapping one roundtrip. The center panel shows the original MRI data. The rightmost panel shows the difference between the two images. The left color scale ranges from the 1^{st} to the 95^{th} percentile of the original concentration data (full range $[-0.517, 0.741]$). The right color scale extends to $\pm 90^{\text{th}}$ percentile of the magnitude of the errors (full range of errors $[-1.10, 0.80]$). Negative concentrations result from noise in image data propagated through the concentration reconstruction algorithm described in Methods. **Lower left:** Alternative visualization of the error introduced by the mapping from MRI image grid to the volume mesh from the 24h session. The leftmost panel shows the MRI image grids' mean concentration within each of the regions defined by the segmentation shown in Fig. 8(d). The middle panel shown the mean concentration of each of the corresponding regions on the mesh, as shown in Fig. 8(f). The third panel shows the difference between the mean concentrations. Range of color scale is shared with upper left figure. **Right:** Scatterplot comparing the regionwise mean concentrations in the MRI image with the corresponding regionwise mean concentrations in the computational mesh, with regions defined by the segmentation shown in Fig. 8(d–f), colored by session. *The individual depicted has provided written consent for inclusion of these images in this manuscript.*

intrathecal injection of contrast agent
(injection into CSF of the spinal canal)

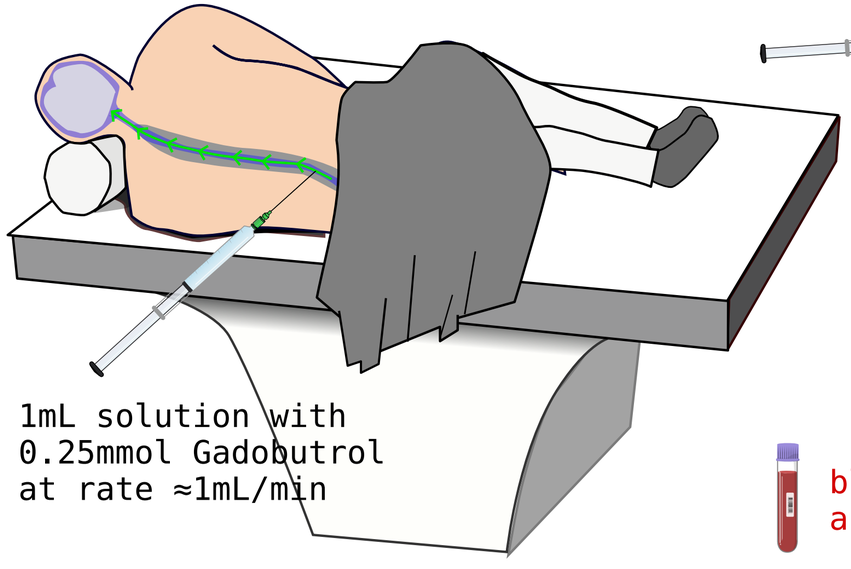

1mL solution with
0.25mmol Gadobutrol
at rate ≈1mL/min

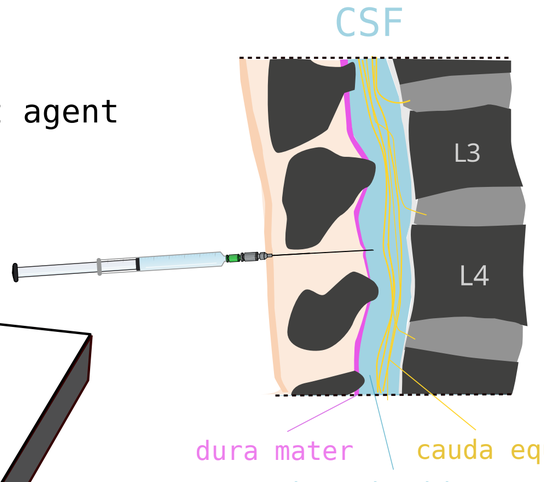

MRI

T1-weighted
Look-Locker
Mixed IR/SE
T2-weighted*
FLAIR*
DTI*

*only pre-contrast

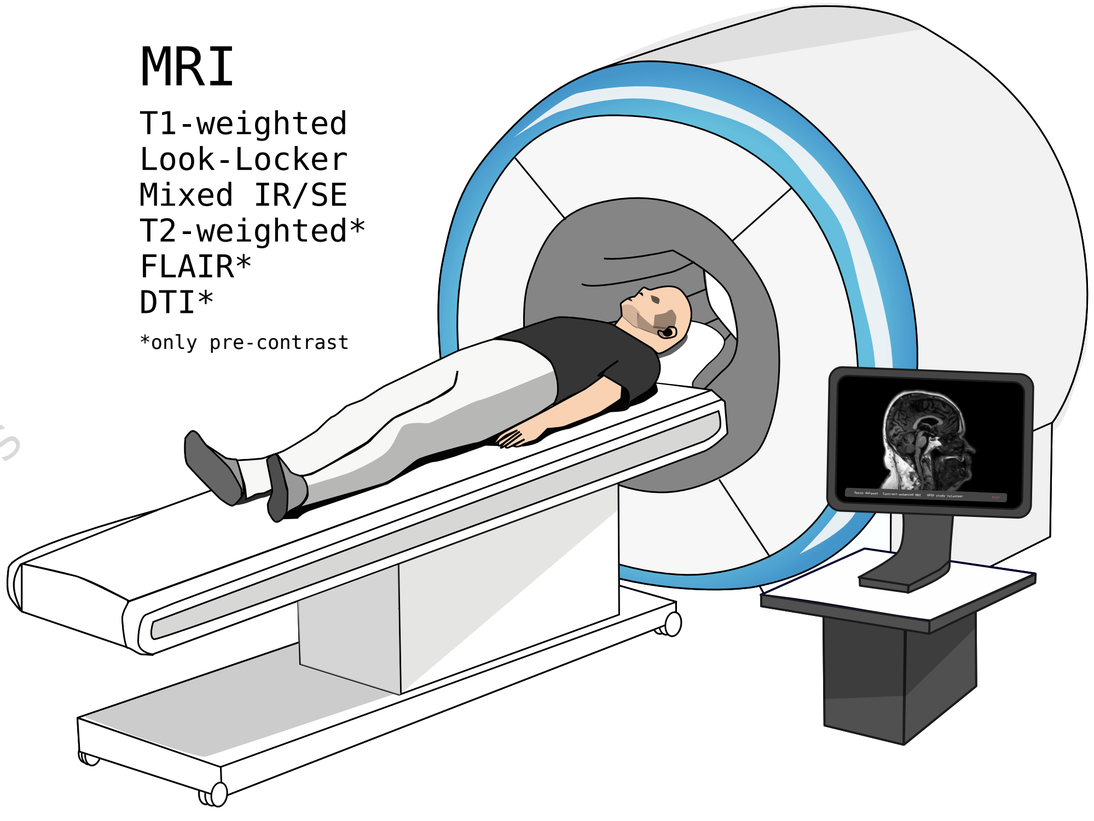

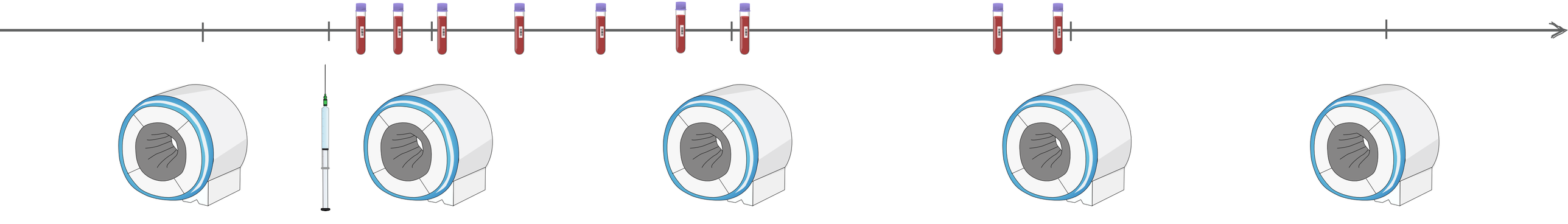

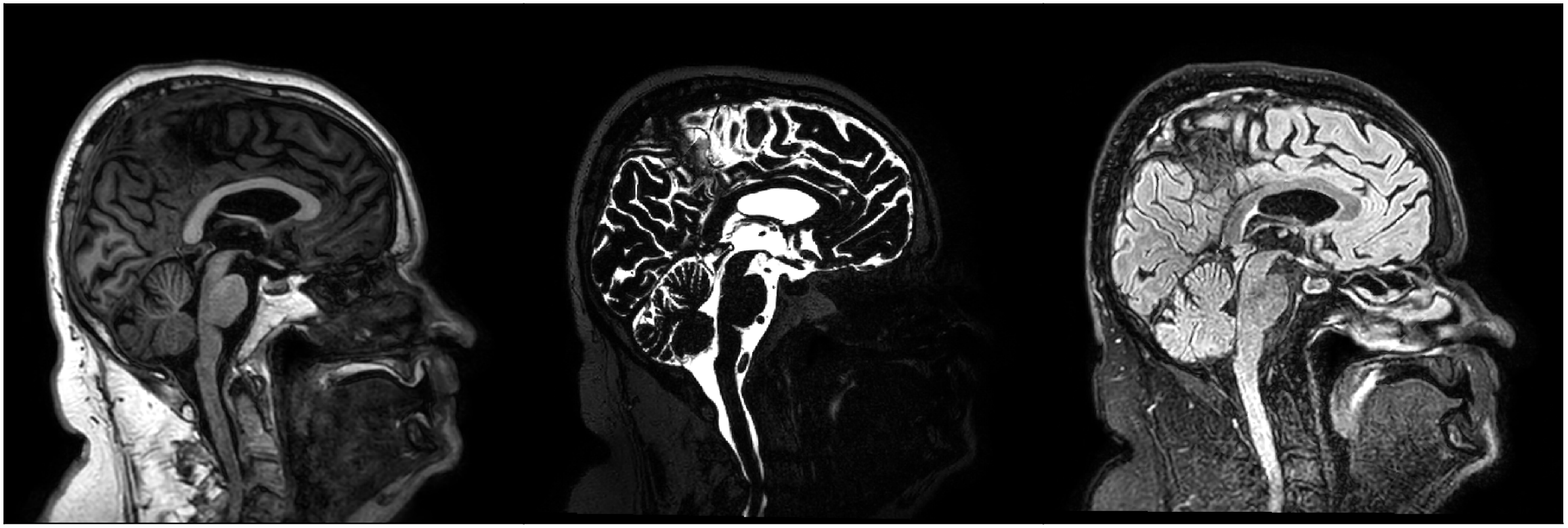
T_1-weighted
T_2-weighted
FLAIR

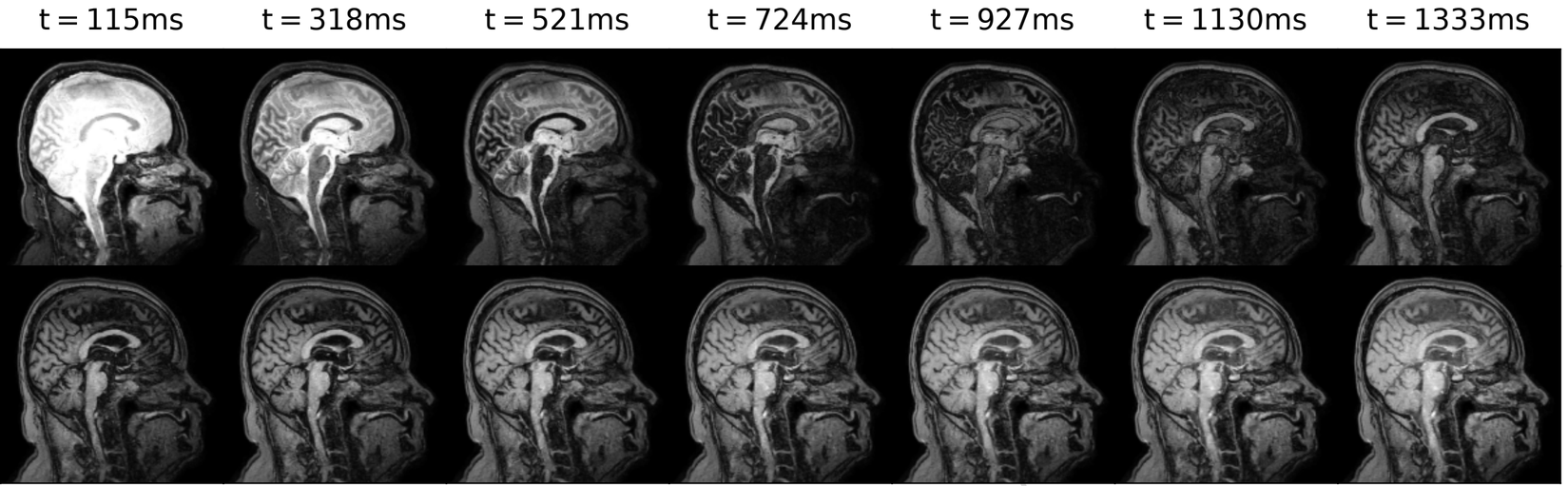
t = 115ms
t = 318ms
t = 521ms
t = 724ms
t = 927ms
t = 1130ms
t = 1333ms
t = 1536ms
t = 1739ms
t = 1942ms
t = 2145ms
t = 2348ms
t = 2551ms
t = 2754ms

(a)

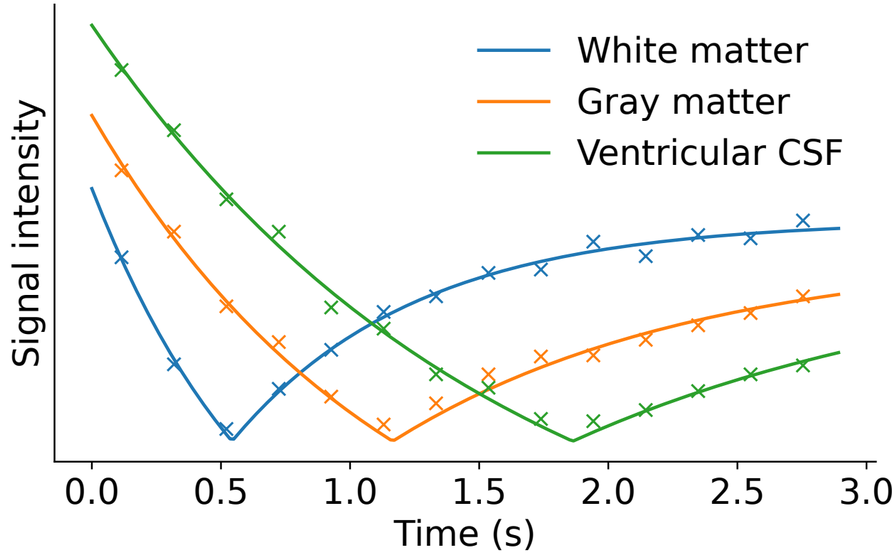
White matter
Gray matter
Ventricular CSF
Signal intensity
0.0
0.5
1.0
1.5
2.0
2.5
3.0
Time (s)

(b)

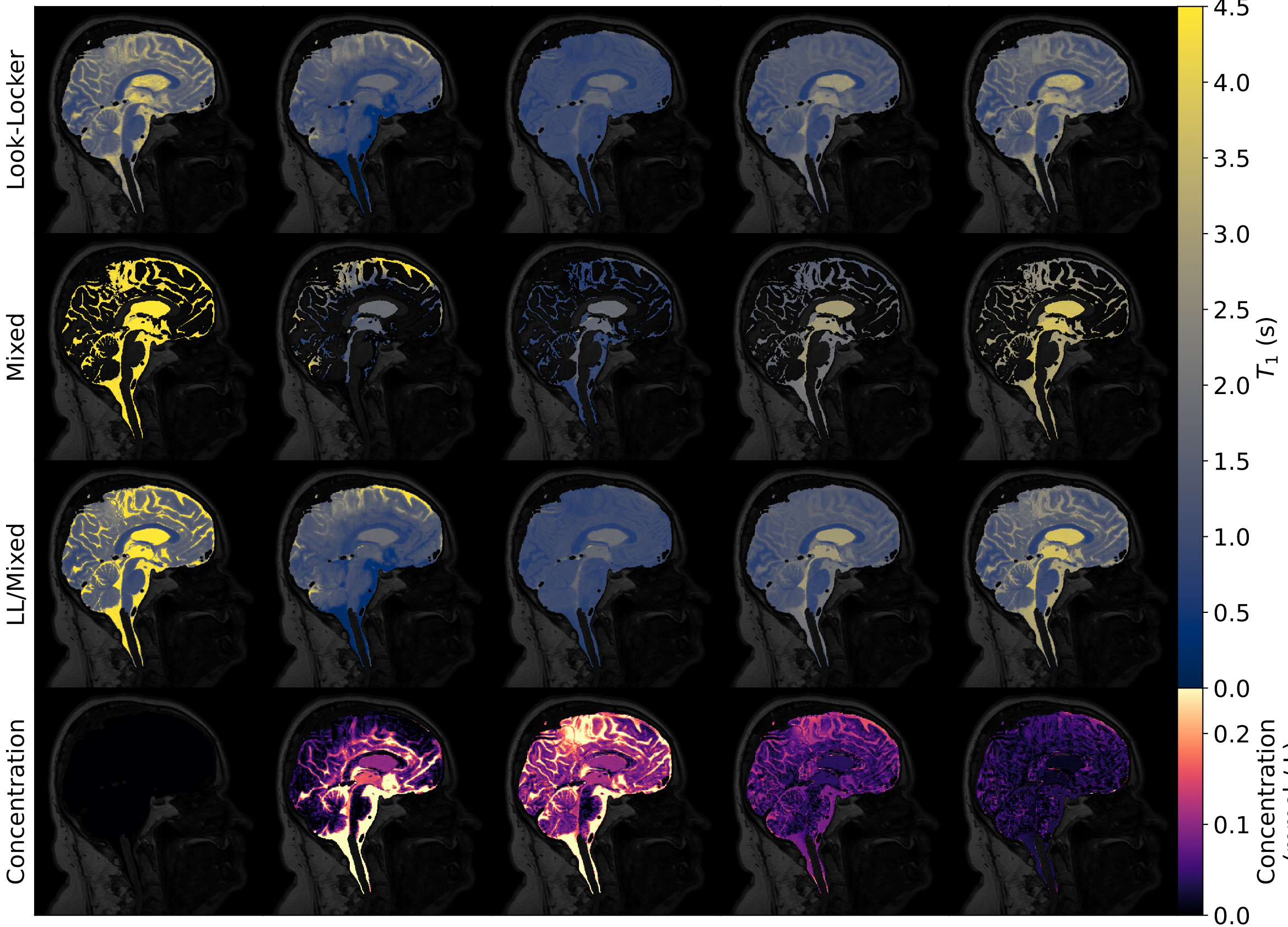
Pre-Contrast
4h
24h
48h
70h
Look-Locker
Mixed
Combined LL/Mixed
Concentration
4.5
4.0
3.5
3.0
2.5
2.0
1.5
1.0
0.5
0.0
T_1 (s)
0.2
0.1
0.0
Concentration (mmol / L)

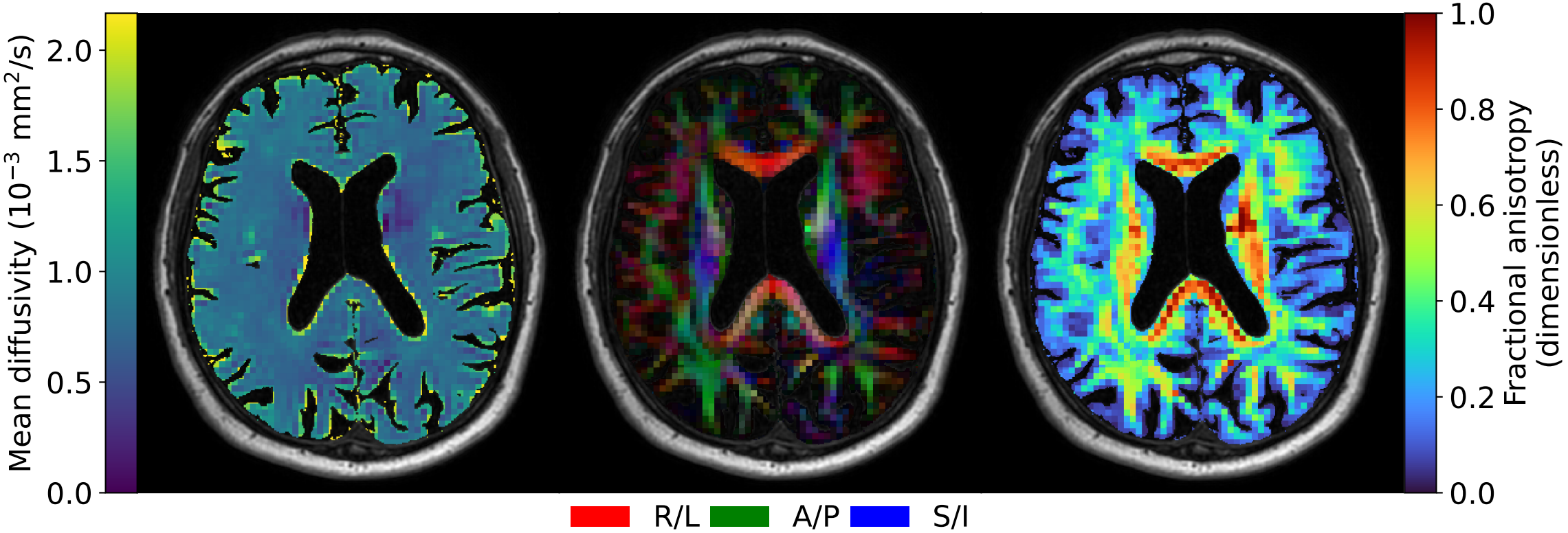
Mean diffusivity (10^{-3} mm^2/s)
2.0
1.5
1.0
0.5
0.0
Fractional anisotropy (dimensionless)
1.0
0.8
0.6
0.4
0.2
0.0
R/L
A/P
S/I

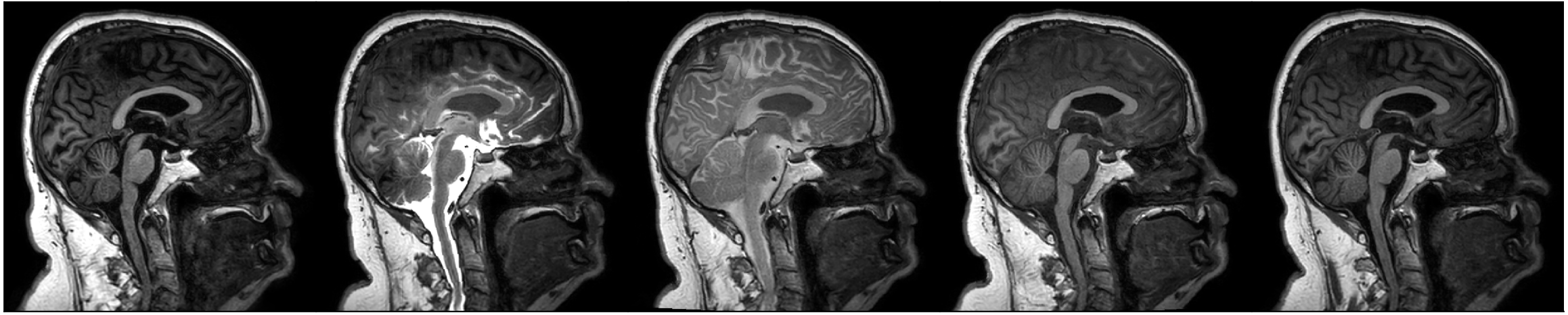

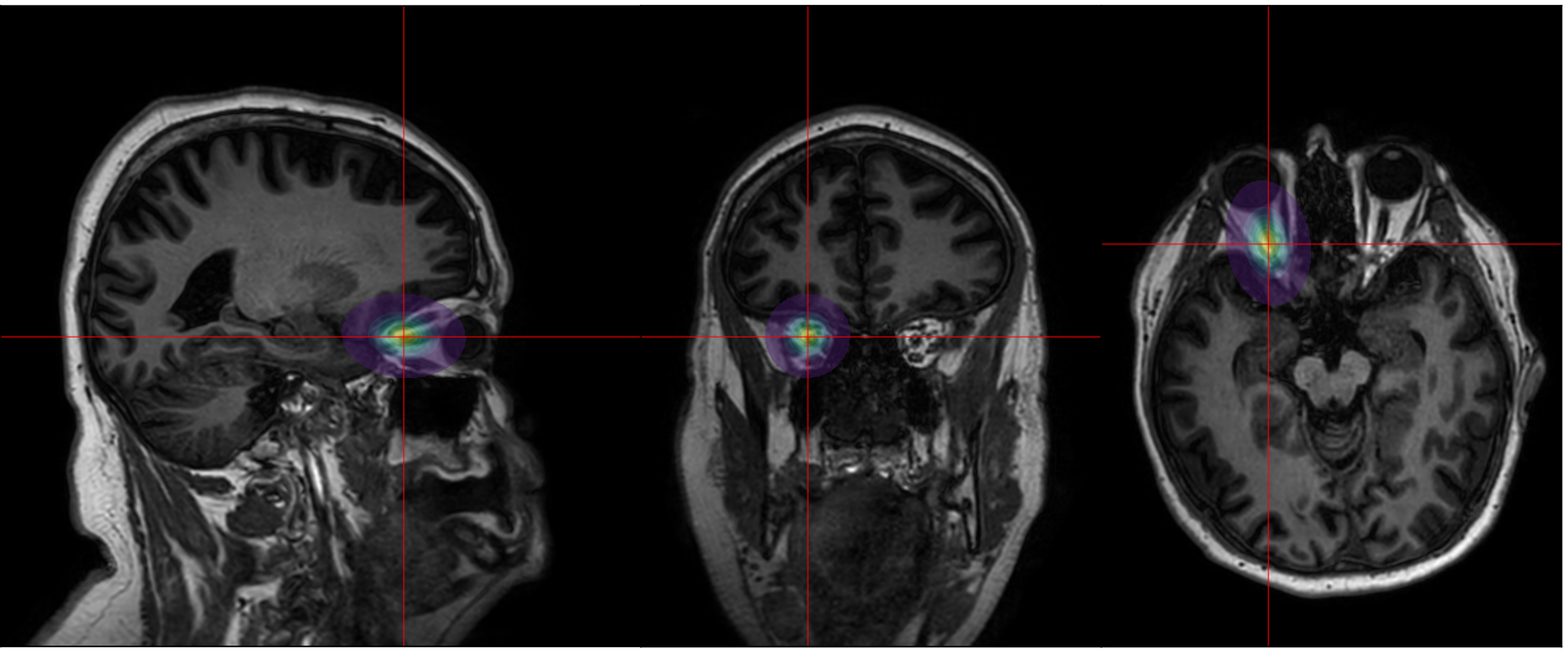

(a)

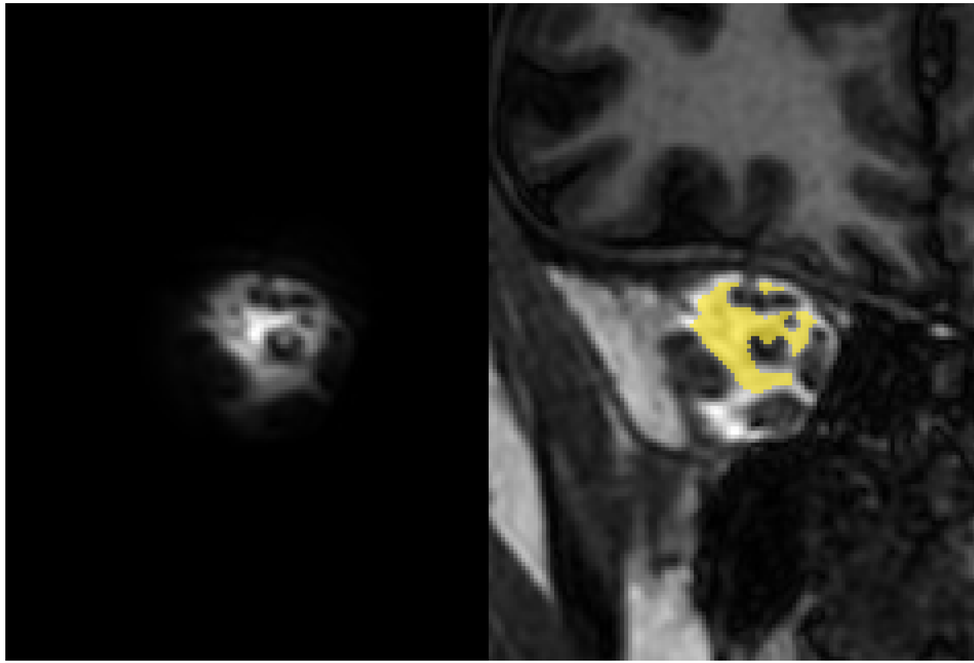

(b)

(a)

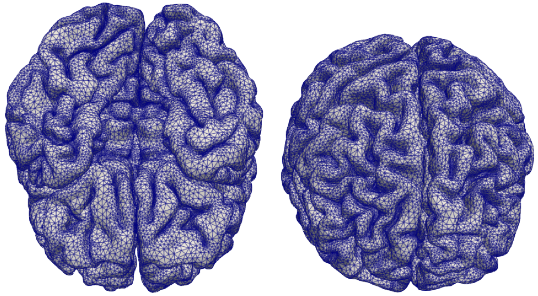

(b)

(c)

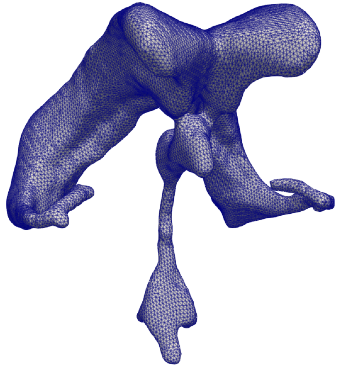

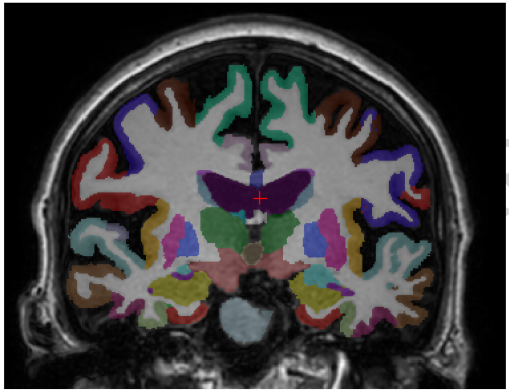

(d)

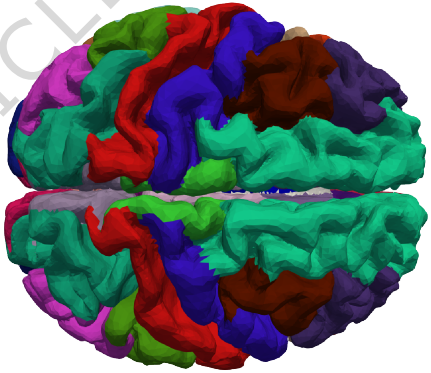

(e)

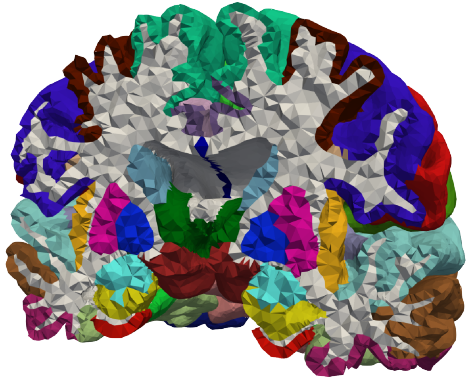

(f)

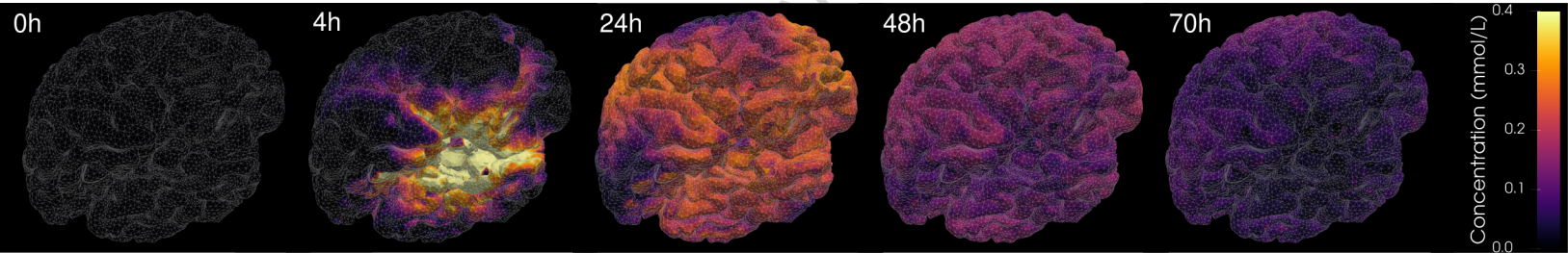

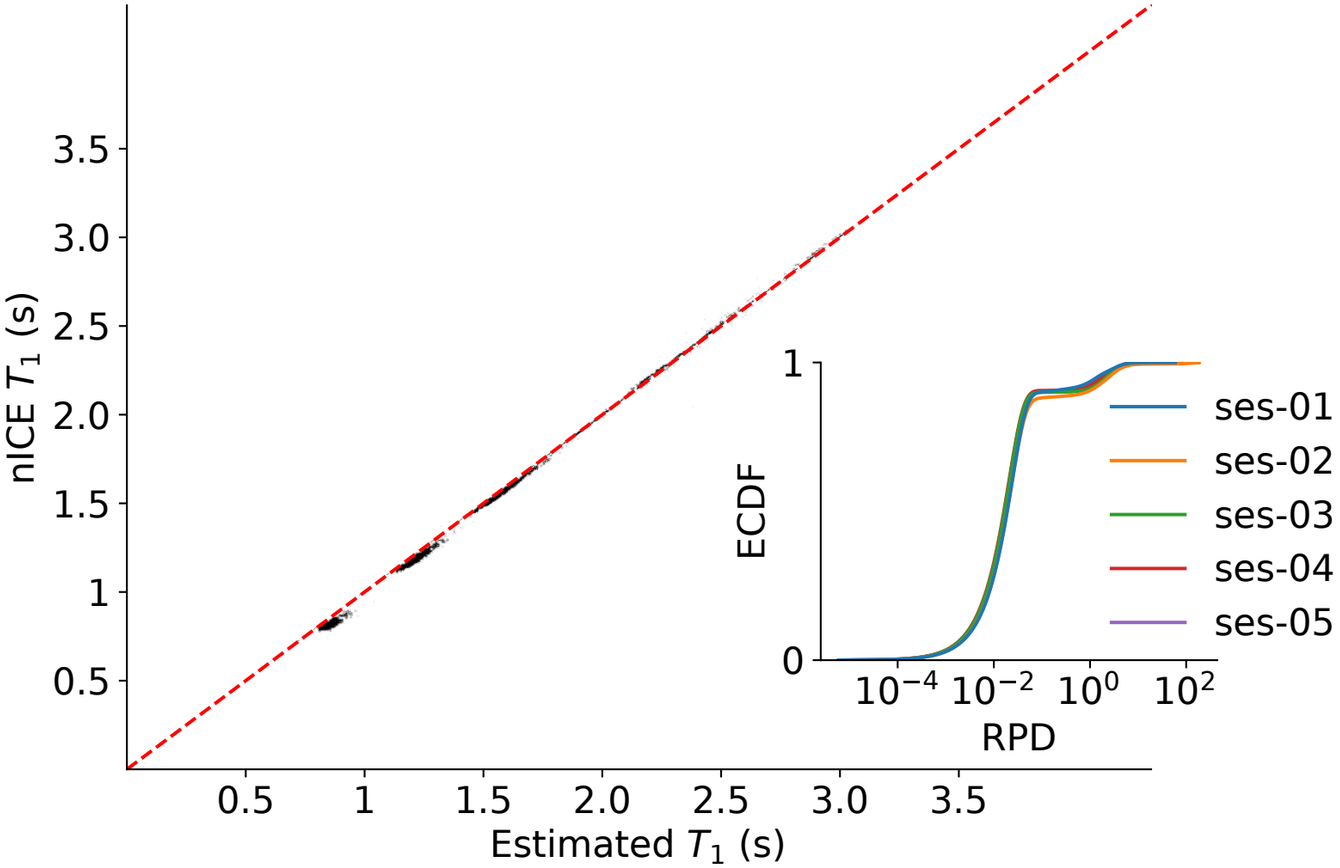
nICE T_1 (s)
Estimated T_1 (s)
ECDF
RPD
ses-01
ses-02
ses-03
ses-04
ses-05

(a)

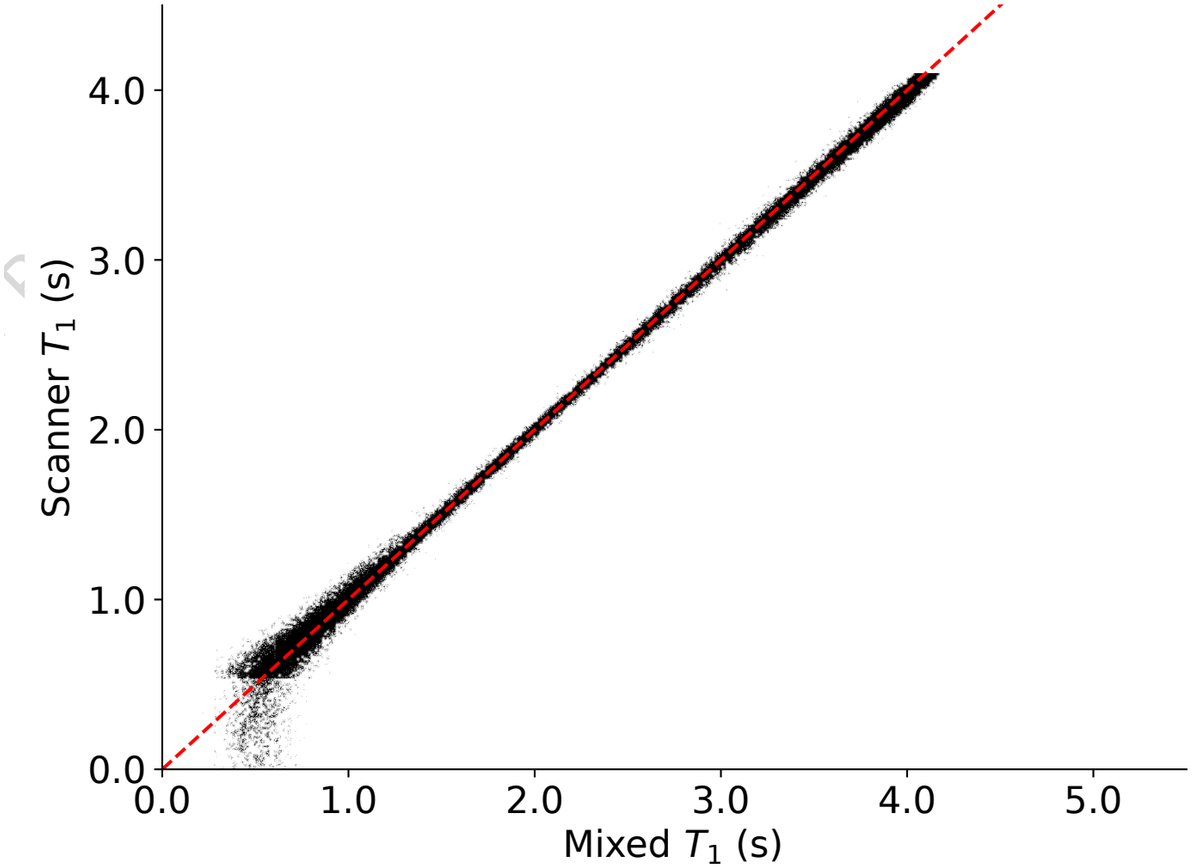
Scanner T_1 (s)
Mixed T_1 (s)

(b)

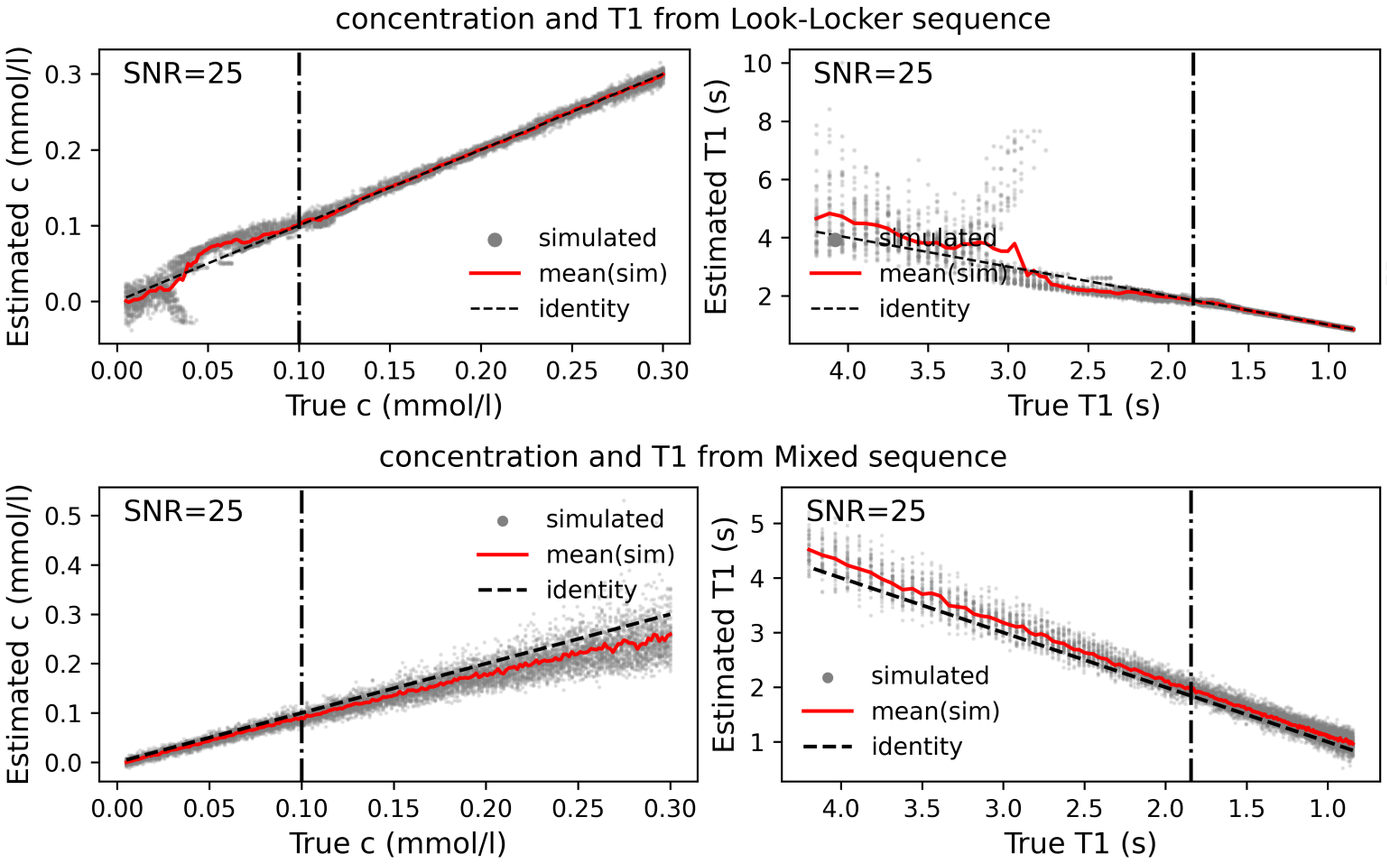
concentration and T1 from Look-Locker sequence
SNR=25
simulated
mean(sim)
identity
Estimated c (mmol/l)
True c (mmol/l)
Estimated T1 (s)
True T1 (s)
concentration and T1 from Mixed sequence
SNR=25
simulated
mean(sim)
identity
Estimated c (mmol/l)
True c (mmol/l)
Estimated T1 (s)
True T1 (s)

(a)

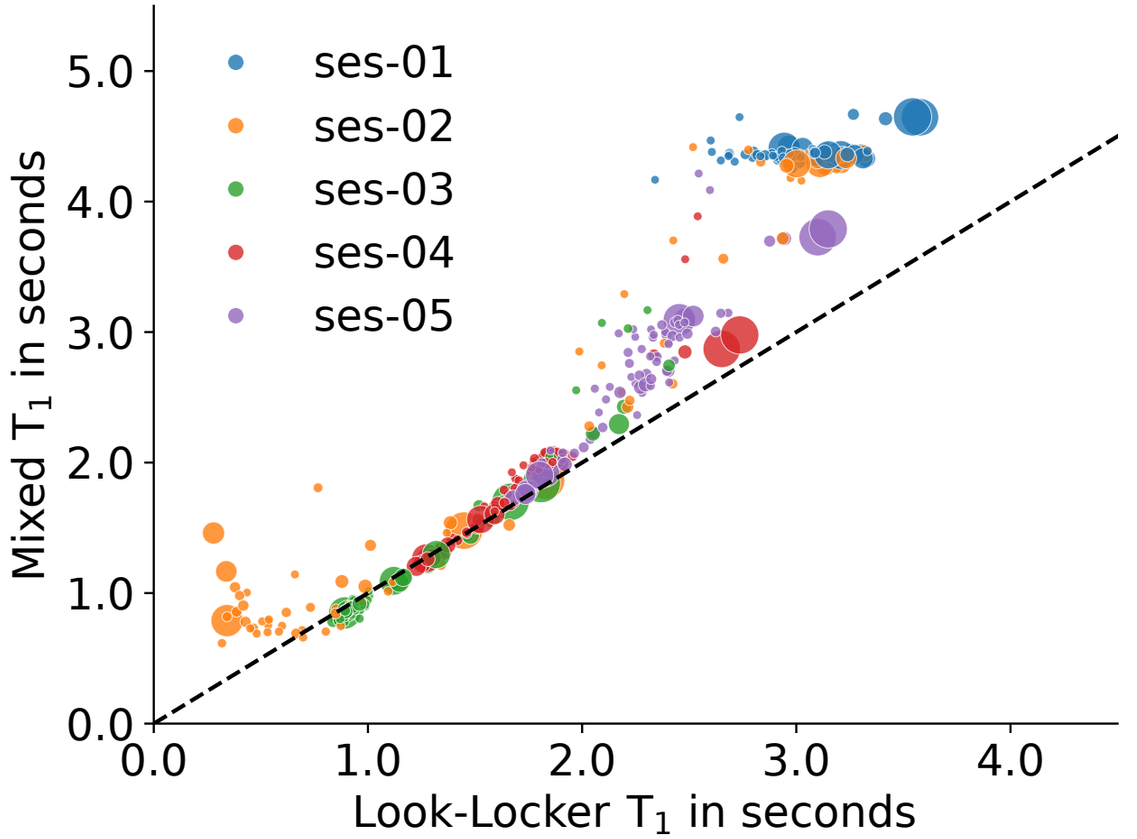
ses-01
ses-02
ses-03
ses-04
ses-05
Mixed T_1 in seconds
Look-Locker T_1 in seconds

(b)

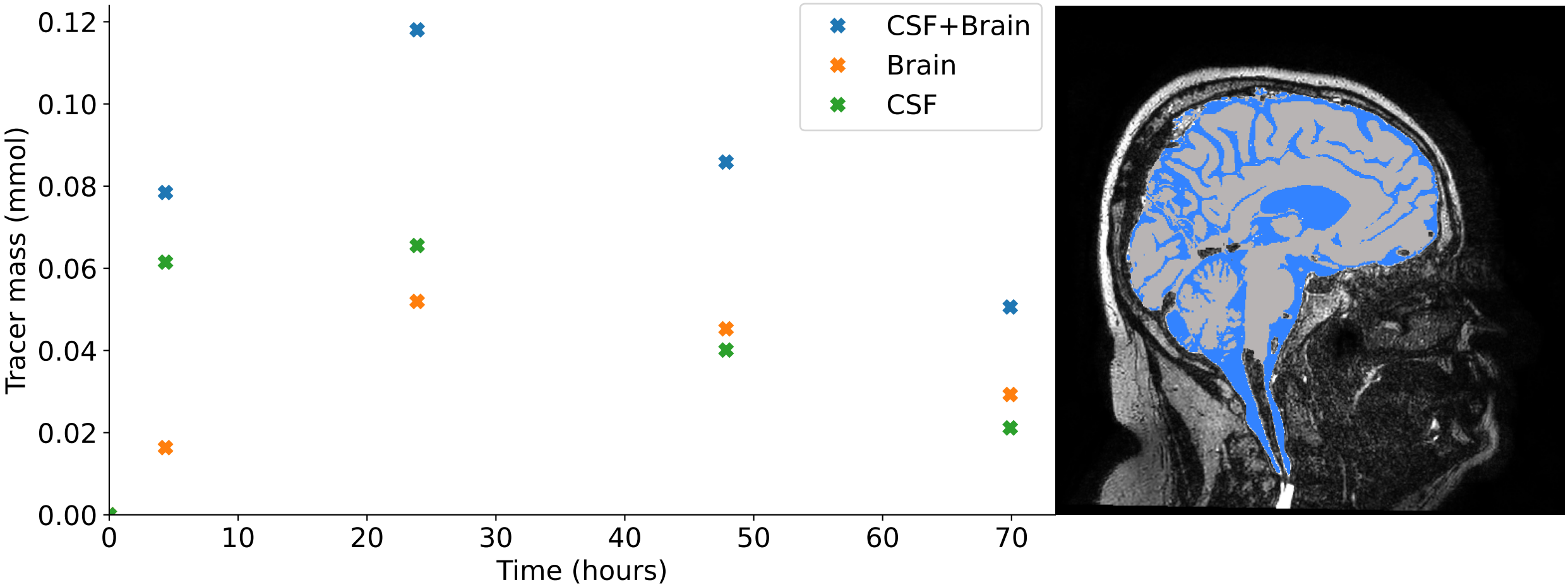
CSF+Brain
Brain
CSF
Tracer mass (mmol)
0.00
0.02
0.04
0.06
0.08
0.10
0.12
0
10
20
30
40
50
60
70
Time (hours)

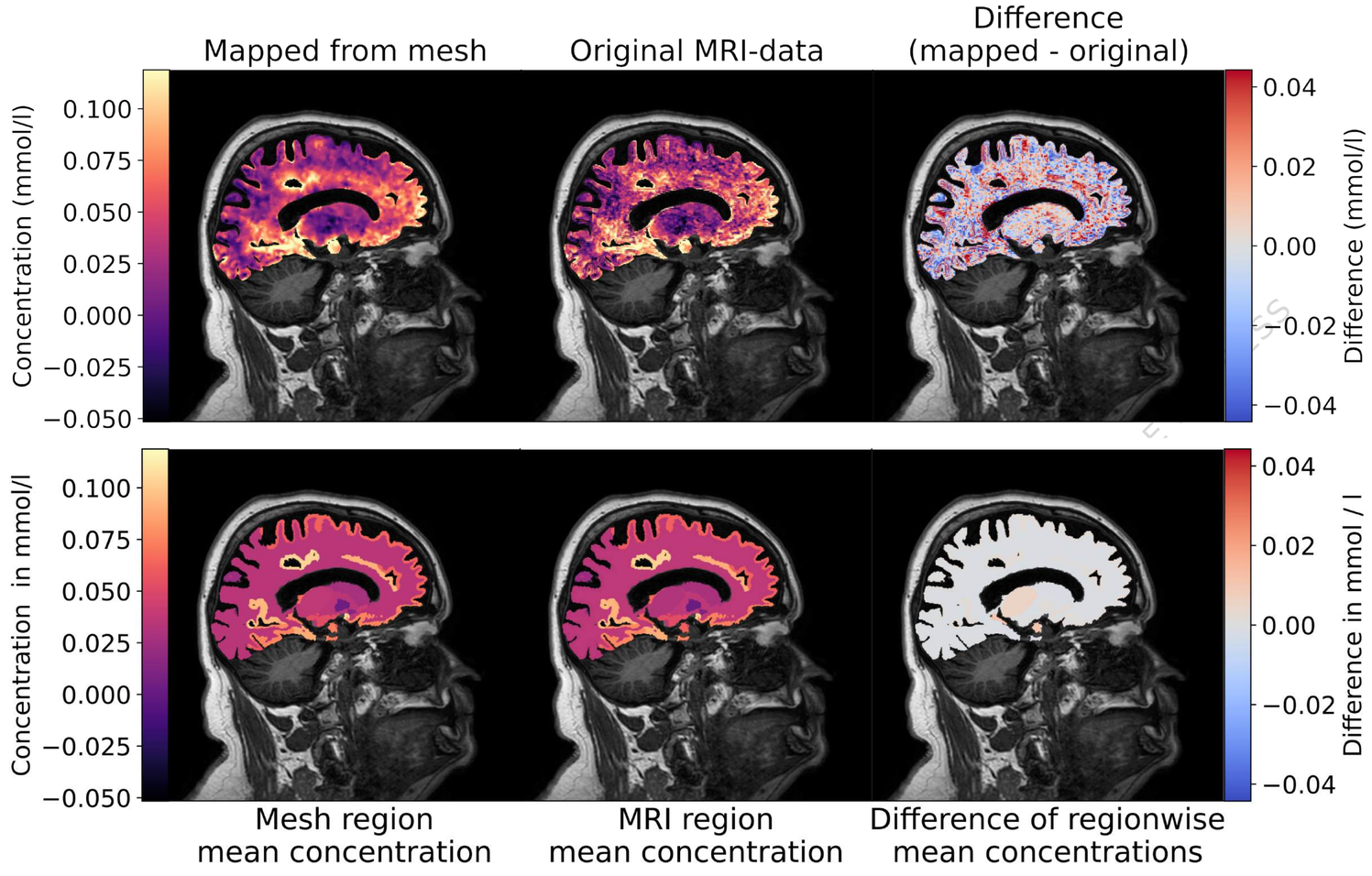
Mapped from mesh
Original MRI-data
Difference
(mapped - original)
Concentration (mmol/l)
0.100
0.075
0.050
0.025
0.000
−0.025
−0.050
0.04
0.02
0.00
−0.02
−0.04
Difference (mmol/l)
Concentration in mmol/l
Difference in mmol / l
Mesh region
mean concentration
MRI region
mean concentration
Difference of regionwise
mean concentrations

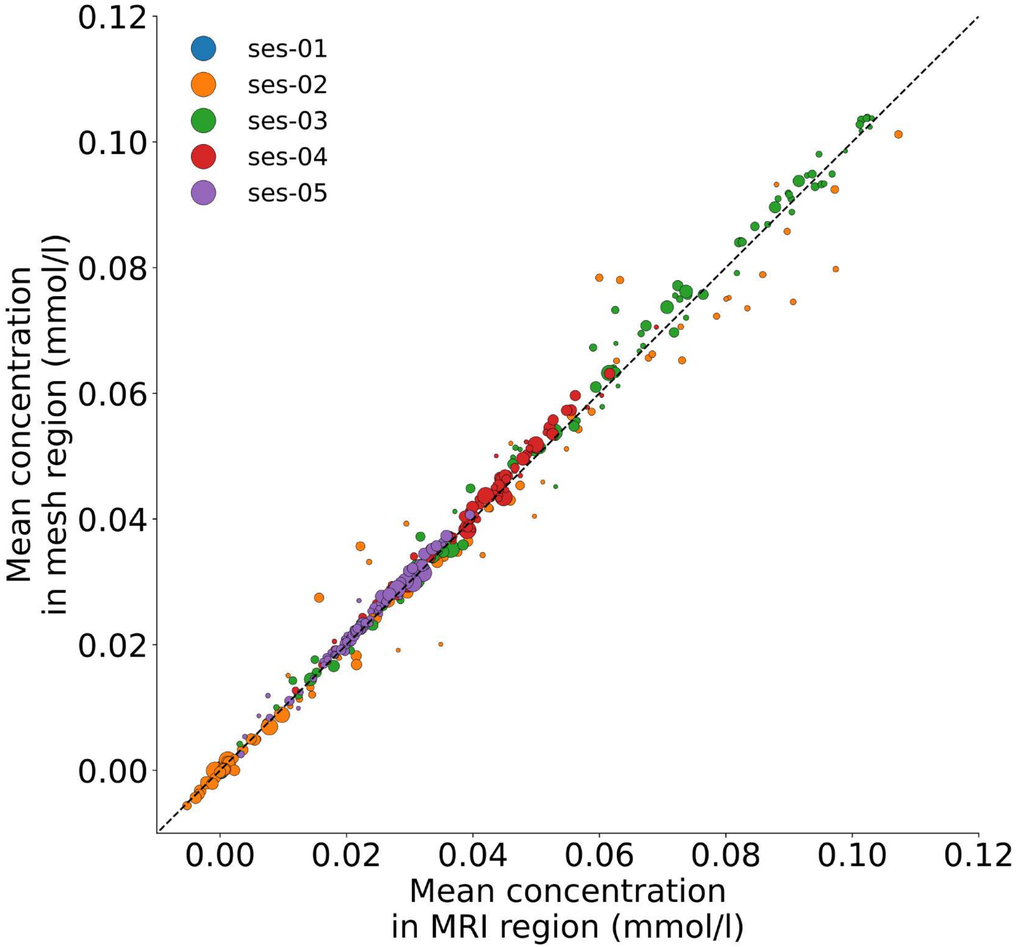
ses-01
ses-02
ses-03
ses-04
ses-05
Mean concentration
in mesh region (mmol/l)
Mean concentration
in MRI region (mmol/l)
0.00
0.02
0.04
0.06
0.08
0.10
0.12